

Benchmark study using a multi-scale, multi-methodological approach for the petrophysical characterization of reservoir sandstones

Peleg Haruzi^{1,2}, Regina Katsman¹, Matthias Halisch³, Nicolas Waldmann¹, and Baruch Spiro^{1,4}

¹ The Dr. Moses Strauss Department of Marine Geosciences, Faculty of Natural Sciences, The University of Haifa, Haifa, Mount Carmel 3498838, Israel

² Agrosphere Institute, IBG-3, Institute of Bio- and Geosciences, Forschungszentrum Jülich GmbH, Germany

³ Leibniz Institute for Applied Geophysics, Dept. 5 – Petrophysics & Borehole Geophysics, Stilleweg 2, D-30655 Hannover, Germany

⁴ Department of Earth Sciences, Natural History Museum, Cromwell Road, London SW7 5BD, UK

Correspondence to: Regina Katsman (rkatsman@univ.haifa.ac.il)

Matthias Halisch (Matthias.Halisch@leibniz-liag.de)

Keywords: multi-methodological approach, permeability, petrography, petrophysics, 3D imaging, pore-scale modelling, upscaling, REV analysis, benchmark study.

Abstract

This paper presents a detailed description and evaluation of a multi-methodological petrophysical approach for the comprehensive multiscale characterization of reservoir sandstones. The suggested methodology enables the identification of links between Darcy-scale permeability and an extensive set of geometrical, textural and topological rock descriptors quantified at the pore scale. This approach is applied to the study of samples from three consecutive sandstone layers of Lower Cretaceous age in northern Israel. These layers differ in features observed at the outcrop, hand specimen, petrographic microscope and micro-CT scales. Specifically, laboratory porosity and permeability measurements of several centimetre-sized samples show low variability in the quartz arenite (top and bottom) layers but high variability in the quartz wacke (middle) layer. The magnitudes of this variability are also confirmed by representative volume sizes and by anisotropy evaluations conducted on micro-CT-imaged 3D pore geometries. Two scales of directional porosity variability are revealed in quartz arenite sandstone of the top layer: the pore size scale of ~ 0.1 mm in all directions, and ~ 3.5 mm scale related to the occurrence of high- and low-porosity horizontal bands occluded by Fe oxide cementation. This millimetre-scale variability controls the laboratory-measured macroscopic rock permeability. More heterogeneous pore structures were revealed in the quartz wacke sandstone of the intermediate layer, which shows high inverse correlation between porosity and clay matrix in the vertical direction attributed to depositional processes and comprises an internal spatial irregularity. Quartz arenite sandstone of the bottom layer is homogenous and isotropic in the investigated domain revealing porosity variability at a ~ 0.1 mm scale, which is associated with the average pore size. Good agreement between the permeability upscaled from the pore-scale modelling and the estimates based on laboratory measurements is shown for the quartz arenite layers. The proposed multi-methodological approach leads to an accurate petrophysical characterization of reservoir sandstones with broad ranges of textural, topological and mineralogical characteristics and is particularly applicable for describing anisotropy and heterogeneity of sandstones on various rock scales. The results of this study also contribute to the geological interpretation of the studied stratigraphic units.

1. Introduction

Permeability is an effective property of a reservoir rock that varies enormously over a wide range of rock length scales, attributed to a hierarchy of dominant sedimentary depositional features (Norris and Lewis, 1991; Nordahl and Ringrose, 2008; Ringrose and Bentley, 2015). Permeability should thus be properly upscaled through the following sequence of scales (Nordahl and Ringrose, 2008; Ringrose and Bentley, 2015 and references therein): (1) from the pore scale (the micro scale, typically microns to millimetres) to the representative elementary volume of a single lamina (the macro scale, typically millimetres to centimetres, e.g., Wildenschild and Sheppard, 2013; Andrä et al., 2013b; Bogdanov et al., 2011; Narsilio et al., 2009); (2) to the scale of geological heterogeneity, e.g., the scale of a stratigraphic unit (decimetres to decametres, e.g., Jackson et al. 2003; Nordahl et al. 2005); and (3) to the field scale or the scale of an entire reservoir or aquifer (hundreds of metres to kilometres) (Haldorsen and Lake 1984; Rustad et al., 2008). Pore scale imaging and modelling enable us to relate macroscopic permeability to basic microscopic rock descriptors (Kalaydjian, 1990; Whitaker, 1986; Cerepi et al., 2002; Haoguang et al., 2014; Nelson, 2009). Therefore, the first stage in the above sequence is crucial for successful upscaling to the overall reservoir scale permeability.

Over the past few decades, 3D pore scale imaging and flow simulations (Bogdanov et al., 2012; Blunt et al., 2013; Cnudde and Boone, 2013; Wildenschild and Sheppard, 2013; Halisch, 2013a) have started to serve as a reliable method for rock characterization. The advantages of these techniques are their non-destructive character and their capability to provide reliable information about the real pore-space structure and topology of rocks that is impossible to obtain using the conventional experimental methods (e.g., Arns et al., 2007; Knackstedt et al., 2010; Blunt et al., 2013). However, despite its importance, the upscaling from the pore scale is sometimes omitted; as a result, effective petrophysical rock characteristics (e.g., porosity, surface area, and permeability) are often evaluated at the macro scale through only conventional laboratory experiments, which often suffer from errors due to local heterogeneities, anisotropy, or an insufficient number of samples (e.g., Meyer, 2002; Halisch, 2013a).

Digital 3D micro scale core analysis should also become a necessary technique for rocks that are difficult to characterize due to various reasons (e.g., for tight sandstones, Liu et al., 2017; Du et al., 2018; Munawar et al., 2018; Zhang et al., 2019), or for those with inhomogeneous or anisotropic pore space (e.g.,

76 Meyer, 2002; Farrel et al., 2014). Preferential fluid flow pathways are inherently connected to rock
77 microstructure, formed by depositional sedimentary structures such as pore shapes and their preferential
78 orientation (Sato et al., 2019) or lamination (Lewis et al., 1988). Those can be modified with time by
79 dissolution of grains, by grain rearrangement and pore collapse (Halisch et al., 2009; Clavaud et al., 2008), by
80 cementation (Louis et al., 2005), or by deformation structures (fractures). The later may drastically alter the
81 host rock depositional porosity pattern and create new permeability pathways (Zhu et al., 2002; Farrel et al.,
82 2014).

83 The present paper provides a detailed description and evaluation of a multi-methodological
84 petrophysical approach for the comprehensive multiscale characterization of reservoir sandstones. The
85 proposed approach includes petrography, gas porosimetry and permeametry, mercury intrusion porosimetry,
86 3D imaging and image analysis, and flow modelling at the pore-scale. The suggested computational workflow
87 enables the identification of Darcy scale permeability links to an extensive set of geometrical, textural and
88 topological rock descriptors, quantified at the pore scale by deterministic methods. The approach presented
89 herein is important for the identification of anisotropy and inhomogeneity. Ultimately, this approach is applied
90 to the study of three different consecutive sandstone layers of Lower Cretaceous age in northern Israel.

91 The multi-methodological validation procedure is significant for properly upscaling permeability from
92 the micro scale to the macro scale (Ringrose and Bentley, 2015). This validation, thereby, allows an accurate
93 petrophysical analysis of reservoir sandstones with broad ranges of textural and topological characteristics.
94 The findings contribute also to the current geological knowledge regarding non-marine sandstones of Lower
95 Cretaceous age (e.g., Akinlotan, 2016; 2017; 2018; Li et al., 2016; Ferreira et al., 2016) and specifically
96 regarding the studied stratigraphic unit.

97

98 **2. Geological setting**

99 The study is based on samples collected from a steep outcrop at Wadi E'Shatr near Ein Kinya on the
100 southern slopes of Mt. Hermon (Figure 1). The outcrop consists of sandstones from the Lower Cretaceous
101 Hatira Formation (Sneh and Weinberger, 2003). This formation (Fm.) acts as a reservoir rock for hydrocarbons
102 in Israel (Figure 1a), both onshore, namely, Heletz (Grader and Reiss, 1958; Grader, 1959; Shenhav, 1971,

103 Calvo, 1992; Calvo et al., 2011), and offshore, namely, Yam Yafo (Gardosh and Tannenbaum, 2014; Cohen,
104 1971; Cohen, 1983).

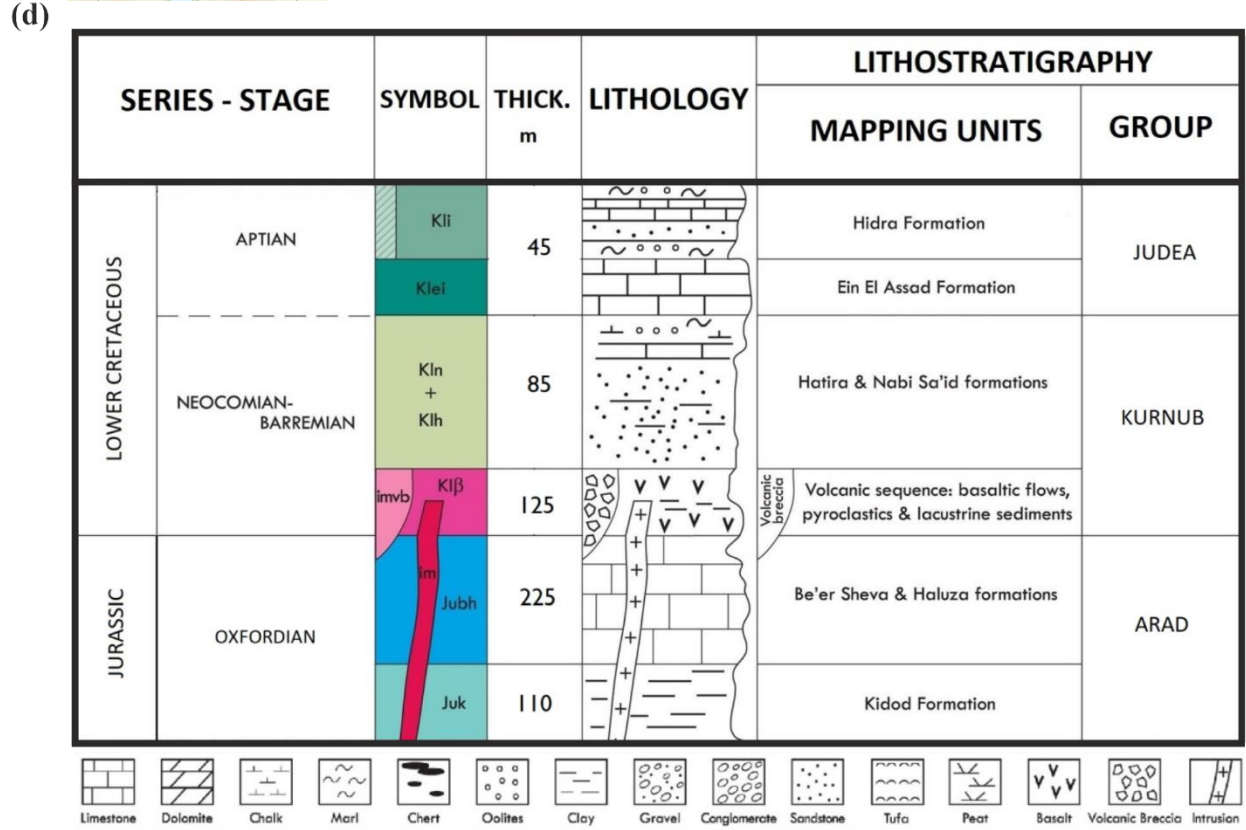
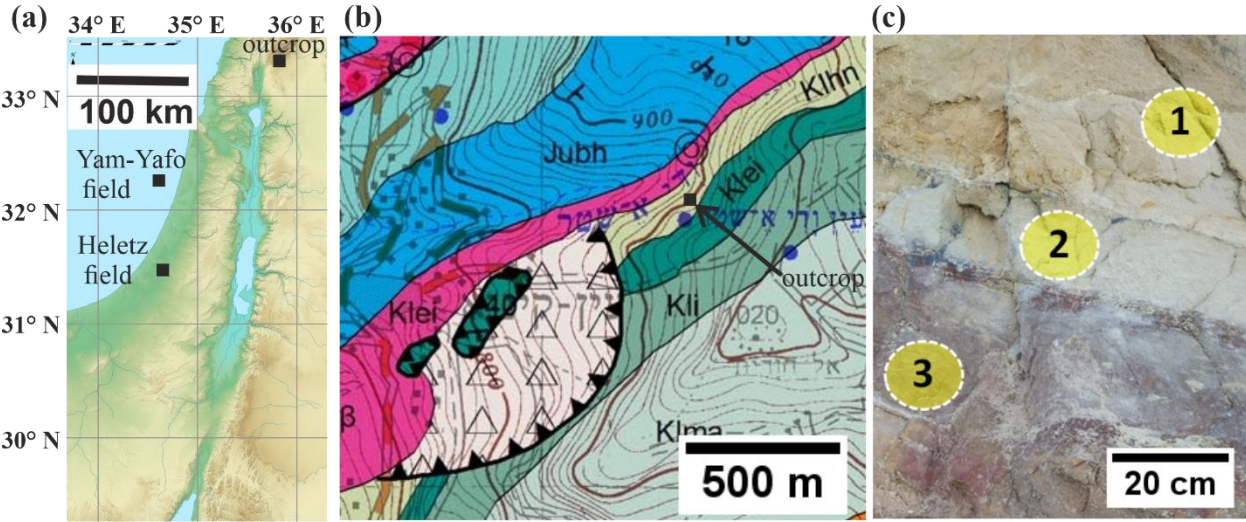
105 The Hatira Fm. is the lower part of the Kurnub Group (Figure 1d) of Lower Cretaceous (Neocomian –
106 Barremian) age. The Hatira Fm. nomenclature used in Israel and Jordan is equivalent to Grès de Base in
107 Lebanon (Massaad, 1976). This formation occurs in Israel in outcrops from the Eilat area along the rift valley,
108 in the central Negev, and in the northernmost outcrops on Mount Hermon; it forms part of a large Palaeozoic
109 – Mesozoic platform and continental margin deposits in north-eastern Africa and Arabia. The Hatira Fm.
110 consists of siliciclastic units, typically dominated by quartz-rich sandstones (Kolodner et al., 2009 and
111 references therein). The underlying Palaeozoic sandstones cover large areas in North Africa and Arabia from
112 Morocco to Oman; these sandstones overlie a Precambrian basement affected by Neoproterozoic (pan African)
113 orogenesis (Garfunkel, 1988, 1999; Avigad et al., 2003, 2005). The lower Palaeozoic sandstones in Israel and
114 Jordan originated from the erosion of that Neoproterozoic basement, the Arabian-Nubian Shield, with
115 contributions from older sources. These lower Palaeozoic sandstones (Cambrian and Ordovician) are
116 described as first-cycle sediments (Weissbrod and Nachmias, 1986; Amireh, 1997; Avigad et al., 2005).
117 Exposures of the Hatira Fm. in the Central Negev, the Arava Valley, Eilat and Sinai were originally defined
118 as the Wadi (Kurnub) Hatira Sandstone (Shaw, 1947). The largely siliciclastic section of the Hatira Fm. is
119 intercalated with carbonates and shales representing marine incursions that increase towards the north
120 (Weissbrod, 2002).

121 The Lower Cretaceous sandstones of the Kurnub Group are described as super mature, cross-bedded,
122 medium- to fine-grained, moderately sorted to well-sorted quartz arenites with a high zircon-tourmaline-rutil
123 (ZTR) index (for more details, see Kolodner, 2009). Earlier observations indicated the relatively scarce
124 occurrence of siltstones and claystones compared to sandstones (Massaad, 1976; Abed, 1982; Amireh, 1997).
125 These Lower Cretaceous sandstones are mainly the recycled products of older siliciclastic rocks throughout
126 the Phanerozoic; the sand was first eroded from the surface of the pan African orogeny ca. 400 Ma prior to its
127 deposition in the Lower Cretaceous sediments (Kolodner et al., 2009).

128 The Mount Hermon block was located at the southern border of the Tethys Ocean during the Early
129 Cretaceous (Bachman and Hirsch, 2006). A paleo-geographical reconstruction indicates that the sandy Hatira
130 Fm. (Figure 1) was deposited in a large basin, which included both terrestrial and coastal environments such

131 as swamps and lagoons (Sneh and Weinberger, 2003). The Hermon block, located next to the Dead Sea
132 Transform, was rapidly uplifted during the Neogene (Shimron, 1998). The area is marked by intense erosion,
133 which resulted in extensive outcrops such as those near Ein Kinya on the south-eastern side of Wadi E'Shatr
134 (Figure 1).

135 The Kurnub Group in the study area (Figure 1b, d) consists of a volcanic sequence at its base that is
136 overlain with an angular unconformity by sandstone and clay layers of the Hatira Fm.; the upper unit consists
137 of limestone, marl and chalk – the Nabi Said Fm. (Sneh and Weinberger, 2003). At the section investigated
138 by Saltzman (1968), which is approximately 100 m SW of the sampling area of the present study, the 58 m
139 thick variegated sandstone is interbedded with layers of clay and clay-marl. The sandy component is white-
140 yellow-brown/red and consists of largely angular, poorly sorted, fine- to coarse-grained quartz sand.
141 Individual sandstone layers are cemented by Fe oxide (Fe-ox). The outcrops show lenticular benches 0.2 m -
142 1.0 m thick. The clay-rich interlayers are grey and normally silty and brittle. Locally, these layers contain
143 lignite. The outcrop investigated and the specific beds sampled in the present study are shown in Figure 1c.



147 are marked as *Klhn* (map is adopted from *Sneh and Weinberger, 2014*). (c) Outcrop of the Lower Cretaceous *Hatira Fm.*
148 sandstones (*Klhn*) at *Ein Kinya*. The studied sandstone layers have distinct colours: yellow-brown (1), grey-green (2),
149 and red-purple (3). (d) Stratigraphic table of the geological map (modified from *Sneh and Weinberger, 2014*).

150 3. Methods

151 3.1. Sample description

152 Samples were extracted from three consecutive layers of different colours from a stratigraphic sequence
153 (Figures 1c, 1d). The lower layer (3) is ~1.5 m thick and consists of sandstone that is light (pale) red-purple in
154 colour with undulating bedding planes between the sub-layers. The middle layer (2) is composed of grey –
155 green shaly sandstone that is 20 cm thick with dark horizons at the bottom and top. The upper layer (1)
156 comprises 1.5 m thick homogenous brown-yellow sandstone. Large sample blocks of ~10-20 cm size were
157 collected from these three layers, and the directions perpendicular to the bedding planes (defined as the z-
158 directions in our study) were noted. Subsequently, in the laboratory, smaller sub-samples (described below)
159 were prepared from these large samples for textural observations and various analytical measurements and
160 computations. In total, 7 sub-samples from the top layer, 8 sub-samples from the middle layer and 4 sub-
161 samples from the bottom layer were investigated in the laboratory (Table 2).

162 3.2. Laboratory and computational methods for rock characterization

163 The integrated analytical programme designed for this study includes the following laboratory
164 measurements and computations conducted at different scales (from the micro scale reflecting the scale of
165 individual pores and grains to the core scale reflecting the scale of the laminas at the outcrop) (Table 1).
166 Specimens ~5-7 cm in size were investigated by petrographic and petrophysical lab methods. Sub-samples ~1
167 cm in size were retrieved from the aforementioned plugs for investigation by 3D imaging, digital image
168 analysis and simulation techniques (described in detail below).

169 Petrographic and petrophysical analysis (#1-7 in Table 1) were conducted following the RP40 guidelines
170 (*Recommended Practices for Core Analysis, API, 1998*), giving detailed information on theory, advantages
171 and drawbacks of each method. An extended computational workflow (#8 in Table 1) combines several
172 methods that may contain some variability in their application for the rock characterization. Those are
173 described in more detail below.

174 **Table 1.** Laboratory methods employed and petrophysical characteristics determined from these methods

Method	Determined petrophysical characteristics
1. Scanning electron microscopy (SEM)	Mineral abundance, grain surface characterization of matrix and cementation
2. Grain size analysis (Laser diffraction)	Grain size distribution (<i>GSD</i>)
3. X-ray diffraction (XRD)	Mineral components
4. Nitrogen gas porosimetry	Porosity (ϕ)
5. Steady state permeametry	Permeability (1D) (κ)
6. Mercury intrusion porosimetry (MIP)	Pore throat size distribution (<i>PTSD</i>), specific surface area (<i>SSA</i>), characteristic length (l_c), pore throat length of maximal conductance (l_{max}), permeability (κ)
7. Optical microscopy Plane-parallelized (PPL) and cross-parallelized (XPL) and reflected-light (RL) microscopy, binocular (BINO).	Mineral abundance, grain surface characterization, cementation
8. Extended computational workflow: Digital image analysis (DIA)	Porosity (ϕ), pore specific surface area (<i>PSA</i>), tortuosity (τ), pore size distribution (<i>PSD</i>), connectivity index (<i>CI</i>), micro-CT predicted porosity from MIP
Fluid flow modelling	Permeability tensor ($\bar{\kappa}$), tortuosity (τ)

175

176 Petrographic descriptions of rock compositions and textures at the micro scale, notably those of the fine
177 fraction, were performed using scanning electron microscopy (*JCM-6000 Bench Top SEM device*; e.g.,
178 Krinsley et al., 2005) using both backscatter and secondary electron modes.

179 Thin-section optical microscopy (*Olympus BX53 device*, e.g., MacKenzie et al., 2017) was used to
180 estimate the mineral abundance and surface features of the grains, and the mineralogical and textural features
181 of matrix and cement. Grain size distributions were determined by a laser diffraction particle size analyser (*LS*

13 320; e.g., Wang et al., 2013). X-ray diffraction (*Miniflex 600 device by Rigaku*; e.g., Asakawa et al., 2020) was applied to powdered samples to determine their mineralogical composition.

Effective porosity and permeability were evaluated on dried cylindrical samples (2.5 cm in diameter and 5-7 cm in length). Effective porosity (ϕ) was measured using a steady-state nitrogen gas porosimeter produced by Vinci Technologies (*HEP-E, Vinci Technologies*; e.g. Viswanathan et al., 2018). Absolute permeability (κ) was measured by using a steady-state nitrogen gas permeameter (*GPE, Vinci Technologies*; e.g., Tidwell et al., 1999).

Mercury intrusion porosimetry (*Micromeritics AutoPore IV 9505*, which considers pore throats larger than 0.006 μm ; e.g., Giesche, 2006) was applied to dried cylindrical samples $\sim 1 \text{ cm}^3$ in size to evaluate the following parameters (Table 1):

- Pore throat size distribution (*PTSD*, Lenormand, 2003).
- Specific surface area (*SSA*): the pore surface to bulk sample volume (Rootare and Prenzlow, 1967; Giesche, 2006).
- Characteristic length (l_c): the largest pore throat width (obtained from the increasing intrusion pressure) at which mercury forms a connected cluster (Katz and Thompson, 1987).
- Pore throat length of maximal conductance (l_{max}): defines a threshold for the pore throat size l at which all connected paths composed of $l \geq l_{max}$ contribute significantly to the hydraulic conductance, whereas those with $l < l_{max}$ may completely be ignored (Katz and Thompson, 1987).
- Permeability (Katz and Thompson, 1987):

$$\kappa = \frac{1}{89} l_{max}^2 \frac{l_{max}}{l_c} \phi S(l_{max}) \quad (1)$$

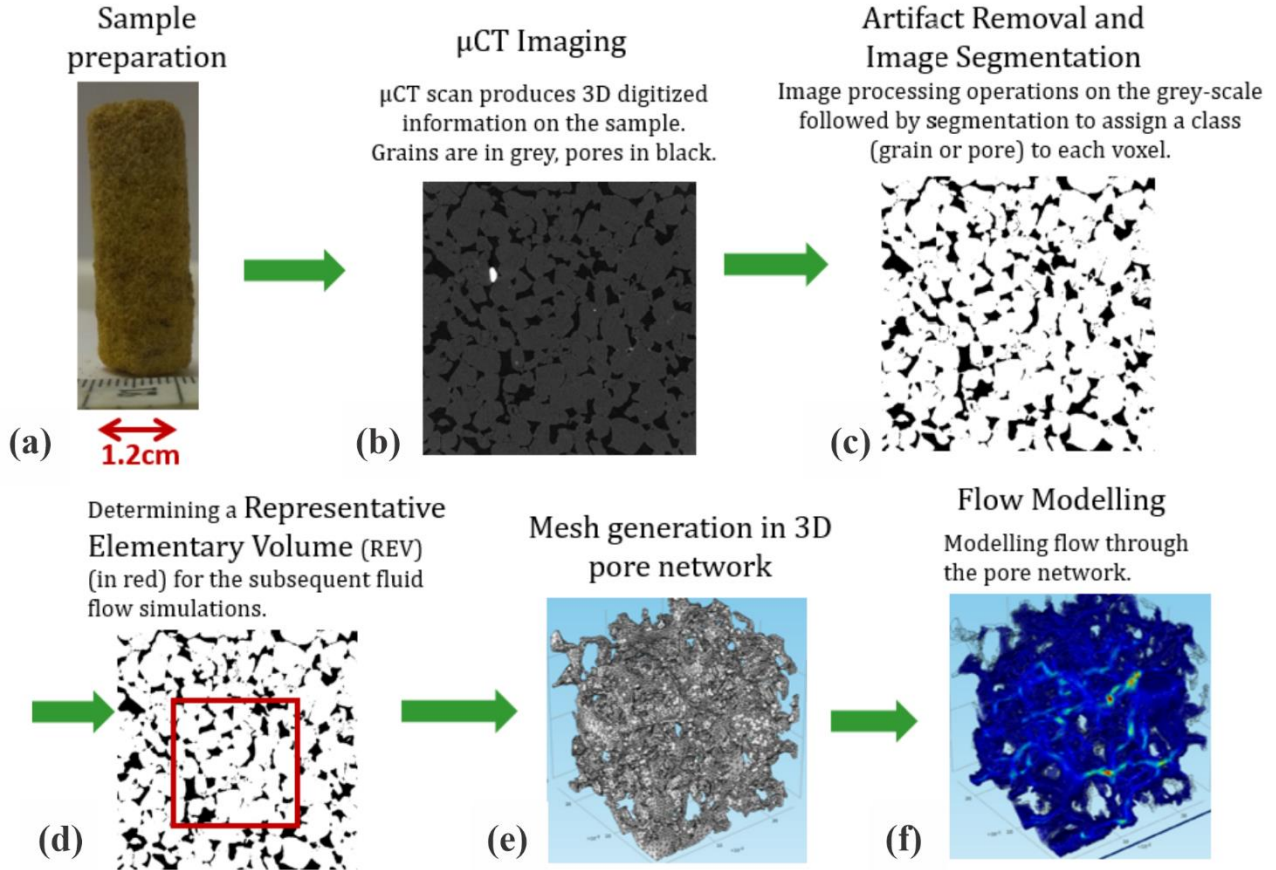
where $S(l_{max})$ is the fraction of connected pore space that is composed of pore throat widths of size l_{max} and larger. This model (Katz and Thompson, 1987), which was derived from percolation theory (Ambegaokar et al., 1971), is applicable for sandstones with a broad distribution of local conductances with short-range correlations only.

An extended computational workflow (similar to the procedure presented by Boek and Venturoli, 2010; Andr  et al., 2013a,b) (Figure 2) serves as one of the main methodologies in our study to upscale permeability

209 and derive microscopic rock descriptors. It includes 3D micro-CT imaging of porous samples, digital image
210 processing and segmentation, statistical analyses for the determination of representative elementary volumes,
211 and pore-scale flow modelling through the 3D pore geometry of the rock. First, cylindrical subsamples 4-8
212 mm in diameter and 5-10 mm in length were retrieved from the larger samples studied in the laboratory (Figure
213 2a) and were scanned non-destructively (Figure 2b) by using a *Nanotom 180 S* micro-CT device (*GE Sensing*
214 *& Inspection Technologies, phoenix/X-ray product line*, Brunke et al., 2008). The achieved voxel size of the
215 data sets was 2.5 μm or 5 μm (isotropic), suitable for imaging pore throats that effectively contribute to the
216 flow in the studied type of sandstone (e.g., Nelson, 2009). Afterwards, all data sets were filtered for de-noising,
217 X-ray artefact removal and edge enhancement (Figure 2c). The post-processed images scanned with 2.5 μm
218 resolution had an edge length of 1180 voxels or 2950 μm . Image artefacts were processed as described by
219 Wildenschild and Sheppard (2013). Beam hardening artefacts were removed by applying the best-fit quadratic
220 surface algorithm (Khan et al., 2016) to each reconstructed 2D slice of the image. Ring artefact reduction and
221 image smoothing (with preservation of sharp edge contrasts) were performed using a non-local means filter
222 (Schlüter, 2014). Segmentation was performed to convert the grey-scale images obtained after image filtering
223 into binary images to distinguish between voids and solid phases (Figure 2c). The local segmentation approach,
224 which considers the spatial dependence of the intensity for the determination of a voxel phase, was used in
225 addition to a histogram-based approach (Iassonov et al., 2009; Schlüter et al., 2014). Segmentation was
226 performed by the converging active contours algorithm (Sheppard et al., 2004), a combination of a watershed
227 (Vincent et al., 1991) with an active contour algorithm (Kass et al., 1988).

228

229
230



231

232 **Figure 2:** Extended computational workflow. See text for more details. Images (e) and (f) are adopted from
233 Bogdanov et al. (2012).

234 Simulations involving the real geometry of an imaged rock are computationally power and time
235 consuming. Therefore, the determination of a representative elementary volume (REV) is required (Figure 2d),
236 assuming that porous media are homogeneous at REV dimensions (Bear, 2013) to perform fluid flow
237 simulations. Porosity, a basic macroscopic structural property of porous media, is used here for the estimation
238 of an REV (Bear, 2013; Halisch, 2013a; Tatomir et al., 2016) based on its correlation with permeability
239 (Kozeny, 1927; Carman, 1937) (see discussion on this issue in the Discussion Sect.).

240 A “classic” REV approach was used that claims that the REV is attained when porosity fluctuations in
 241 the sub-volumes that grow isotropically in three orthogonal directions become sufficiently small (Bear, 2013;
 242 Halisch, 2013a, b). Practically, a large number of randomly distributed cubes were analysed through the entire
 243 3D sample for their image porosity (IP). The chosen initial cube size (with an edge length of 10 pixels in our
 244 case) was increased by 10-100 voxels. The REV size was specified when agreements between the mean and
 245 median IP values as well as saturation in the IP fluctuations were attained.

246 Further, the representative binary 3D image (REV) of the pore space was spatially discretised by
 247 tetrahedrals with *Materialize software (Belgium)* (Figure 2e). This step is required for importing the REV into
 248 the FEM-based modelling software (*Comsol Multiphysics simulation environment*, v5.2a). Stokes flow ($Re \ll$
 249 1) is simulated (Table 1) in the pore network (Figure 2f) by the following equations (e.g., Narsilio et al., 2009;
 250 Bogdanov et al., 2011):

$$251 \quad \text{Stokes equation:} \quad -\nabla p + \mu \nabla^2 \bar{u} = 0 \quad (2)$$

$$252 \quad \text{Continuity equation:} \quad \nabla \cdot \bar{u} = 0 \quad (3)$$

253 where ∇p is the local pressure gradient, \bar{u} is the local velocity vector in the pore space and μ is the dynamic
 254 fluid viscosity. Fixed pressures ($p=const$) were specified at the inlet and outlet boundaries of the fluid domain
 255 with a constant pressure gradient of 2.424 Pa/mm over the domain, prescribed in all the simulations for
 256 consistency. At the internal pore walls and at the lateral domain boundaries, no-slip boundary conditions ($\bar{u} =$
 257 0) were imposed (e.g., Guibert et al., 2016). These boundary conditions are also used to simulate the flow
 258 setup in a steady-state experimental permeameter (e.g., Renard et al., 2001). The macroscopic fluid velocity
 259 $\langle \bar{v} \rangle$ was evaluated by volumetrically averaging the local microscopic velocity field (e.g., Narsilio, 2009;
 260 Guibert et al., 2016). Then, from the average macroscopic velocity vectors v_i^j in three orthogonal i -directions
 261 corresponding to the pressure gradients ∇p_j imposed in j -directions, the full 3D second rank upscaled
 262 permeability tensor $\bar{\kappa}$ can be found:

$$263 \quad \begin{pmatrix} v_x^x & v_x^y & v_x^z \\ v_y^x & v_y^y & v_y^z \\ v_z^x & v_z^y & v_z^z \end{pmatrix} = -\frac{1}{\mu\phi} \begin{pmatrix} \kappa_{xx} & \kappa_{xy} & \kappa_{xz} \\ \kappa_{yx} & \kappa_{yy} & \kappa_{yz} \\ \kappa_{zx} & \kappa_{zy} & \kappa_{zz} \end{pmatrix} \begin{pmatrix} \nabla p_x & 0 & 0 \\ 0 & \nabla p_y & 0 \\ 0 & 0 & \nabla p_z \end{pmatrix} \quad (4)$$

264 where z-direction of the CT specimen used in this analysis is perpendicular to the natural layering of the
 265 sandstone identified in the outcrop and in the petrographic observations. x- and y- orthogonal directions lie in
 266 the horizontal plane, with an azimuth chosen randomly. The permeability tensor is symmetrized by:

$$267 \quad \bar{\kappa}_{sym} = \frac{1}{2}(\bar{\kappa} + \bar{\kappa}^T) \quad (5)$$

268 Additional permeability tensor simulations in the multiple REV sub-volumes of one of the investigated
 269 samples have been performed by using the FlowDict module (Linden et al., 2015; 2018) of the GeoDict toolbox
 270 (Wiegmann, 2019). Pre-processing as well as boundary conditions are identical to those used in Comsol setup.

271 Tortuosity (τ ; Bear, 2013; Boudreau, 1996) was calculated separately in the x-, y- and z-directions in
 272 the meshed domain using the particle tracing tool of *Comsol Multiphysics software* (an additional method for
 273 deriving τ is presented later in this section).

274 3D image analysis (Table 1) was conducted on a high-quality, fully segmented micro-CT image (edge
 275 length of 2950 μm scanned at a 2.5 μm voxel size). Non-connected void clusters in the binary specimen were
 276 labelled and then separated into objects (single pores and grains) by using a distance map followed by the
 277 application of a watershed algorithm (e.g., Brabant et al., 2011; Dullien, 2012). Image analysis operations were
 278 assisted by *Fiji-ImageJ software* (Schindelin et al., 2012) and by the *MorphoLibJ plug-in* (Legland et al.,
 279 2014). The following geometrical descriptors were derived from the segmented image limited by the image
 280 resolution of 2.5 μm (Table 1):

- 281 • micro-CT image porosity (IP);
- 282 • Pore specific surface area (PSA – surface to pore volume);
- 283 • Tortuosity: evaluated in the x-, y- and z-directions by finding the average of multiple shortest paths
 284 through the main pore network using the fast marching method (Sethian, 1996) implemented using an
 285 accurate fast marching plug-in in MATLAB.
- 286 • Pore size distribution (PSD): obtained by a Feret maximum calliper (Schmitt et al., 2016).
- 287 • Euler characteristic (χ) - a topological invariant (Wildenschild and Sheppard, 2013; Vogel, 2002) that
 288 describes the structure of a topological space (see Supplementary material for more detail). Since the
 289 number of pore connections depends on the number of grains (N), it is essential to normalize χ (Scholz
 290 et al., 2012) to compare the connectivity among three samples that have the same dimensions but

different grain sizes. Thus, a Connectivity Index (*CI*) parameter, $CI = |\chi|/N$ was defined, where χ and N were computed using image analysis.

Table 1 allows conducting a comparison between the characteristics derived by the different methods at the different scales of investigation (similarly to Table 1 in Tatomir et al. (2016) that focuses on the similar rock).

Additionally, we propose a new simple method to estimate the image porosity at a given resolution. Multiplication of the mercury effective saturation at the capillary pressure corresponding to the micro-CT resolution (e.g., 2.5 μm) by the porosity of the same sample measured by a gas porosimeter yields the *micro-CT-predicted image porosity from MIP* at the given resolution limit (Table 1).

4. Results

4.1. Petrographic and petrophysical rock characteristics

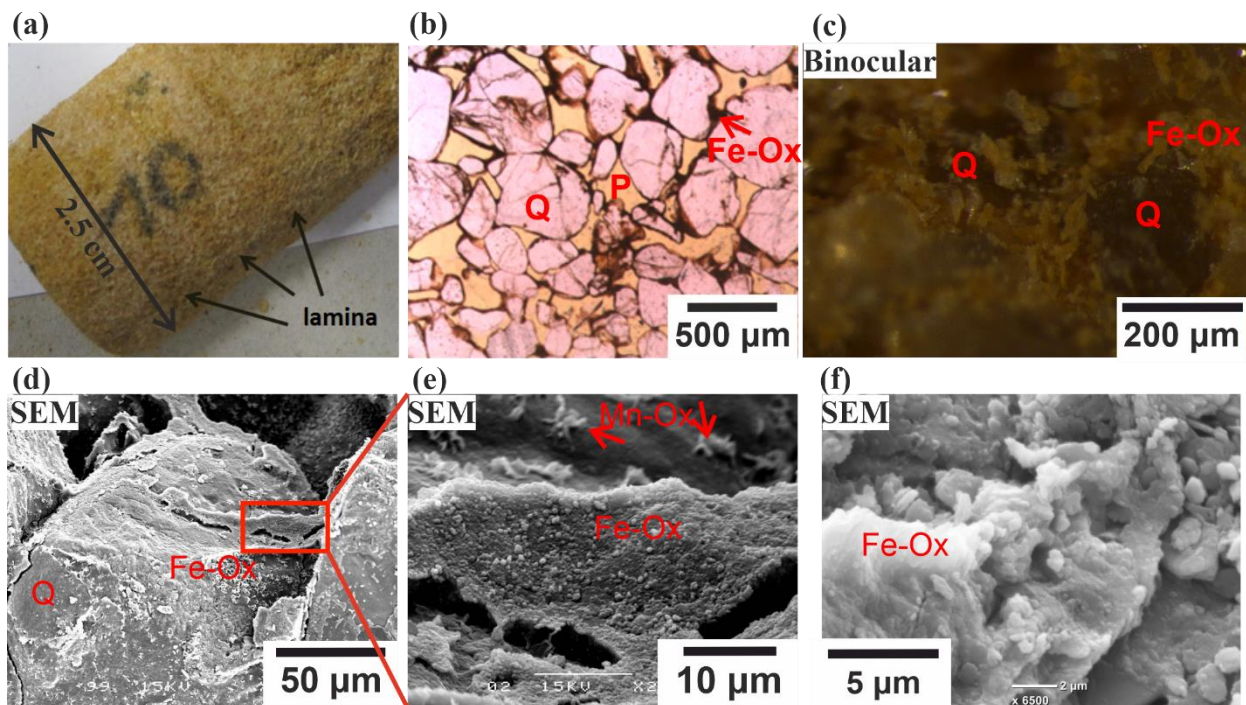
Three types of sandstone rocks were characterized by techniques 1-8 listed in Table 1. The results are presented in Figures 3-8 and summarized in Table 2.

Sandstone S1: The top unit layer with a thickness of ~1.5 m (Figure 1c) consists of yellow-brown sandstone (Figure 3a), which is moderately consolidated. The sandstone is a mature quartz arenite (following Pettijohn et al., 1987) with minor Fe-ox, feldspar and heavy minerals (e.g., rutile and zirconium). The grain size distribution has a mean of ~325 μm (Figure 6a, Table 2). The grains are moderately sorted (according to the classification of Folk and Ward, 1957) and sub-rounded to well-rounded with local thick (millimetre-scale), relatively dark envelopes (Figure 3b). The sandstone consists of alternating millimetre-scale layers of large and small sand grains. Secondary silt (~45 μm) and clay (~0.95 μm) populations are detected in the grain size distribution (Figure 6). X-ray diffraction detected a small amount of kaolinite. The Fe-ox grain-coating and meniscus-bridging cement is composed of overgrown flakes aggregated into structures ~10 μm in size (Figure 3c-3f). Mn oxide is also evident but is scarce (Figure 3e).

The pore network is dominated by primary inter-granular well-interconnected macro porosity (Figure 3b). However, sealed and unsealed cracks in grains are also observed. Higher Fe-ox cementation at the millimetre scale on horizontal planes is recognized (Figure 3a). In addition, smaller voids between Fe-ox aggregates and flakes occur at the micrometre scale and smaller (Figure 3d-f).

The pore throat size analysis conducted with MIP shows that 82 % of the pore volume is composed of macro pores (>10 μm) following a log-normal distribution with a peak at 44 μm (Figure 7a). The characteristic length, i.e., the largest pore throat length at which mercury forms a connected cluster, is $l_c = 42.9 \mu\text{m}$ (Figure 7b), and the pore throat length of maximal conductance is $l_{max} = 34.7 \mu\text{m}$ (Figure A1 in Appendix A). The porosity evaluated by laboratory gas porosimetry varies in the range of 26-29 % for 7 different samples of S1 (Figure 8). Multiplying the mercury effective saturation (85.8 %) at the micro-CT resolution (2.5 μm) (Figure 7a, red dashed line) by the porosity of the same sample measured by gas porosimetry (27.3 %) yields a micro-CT-predicted image porosity of 23.5 % at a resolution limit of 2.5 μm (Table 2).

329 The permeability evaluated by a laboratory gas permeameter has averages of 350 mD (range of 130-
 330 500 mD) for 5 samples measured perpendicular to the depositional plane (z-direction) and 640 mD for 2
 331 samples measured parallel to the depositional plane (x- and y-directions) (Figure 8). MIP measurement (Katz
 332 and Thompson, 1987) yields a permeability (see Sect. 3.2) of 330 mD (Table 2).



333
 334 **Figure 3:** Representative images of sandstone S1. (a) Darker laminae in the x-y plane at the millimetre scale are observed.
 335 (b) Thin section image of S1, P refers to open pores, Q – to quartz, Ox to oxide. (c) Fe-ox flakes (yellow) on quartz grains
 336 (pale grey). (d) SEM image of S1: grain-coating, meniscus-bridging cement and overgrowth of Fe-ox flakes. (e,f)
 337 Magnified images at different scales.

340 **Table 2.** Petrophysical characteristics of the three studied sandstone layers.

	Method	S1	S2	S3
Grain size	Laser diffraction	325 µm medium sand moderately sorted sand: 92.6 % silt: 6.6 % clay: 0.8 %	154 µm very fine sand poorly sorted 65.7 % 31.3 % 3 %	269 µm fine sand moderately sorted 94.4 % 4.8 % 0.8 %
Pore throat size	MIP	Mode 1: 44 µm Mode 2: 0.035 µm Mode 3: 2.2 µm macro pores well sorted	0.035 µm 3.5 µm meso pores poorly sorted	35 µm 0.035 µm 2.2 µm macro pores well sorted
Pore size	Image analysis (min. object size 2.5 µm)	194 µm (FWHM [150,335] µm)	Mode 1: 21 µm Mode 2: ~100 µm	223 µm (FWHM [145,400] µm)
Characteristic length, l_c	MIP	42.9 µm	12.3 µm	36.9 µm
l_{max} contributing to maximal conductance	MIP	34.7 µm	8 µm	31.4 µm
Porosity, ϕ	Gas porosimetry	$28 \pm 2 \%$ (7)	$19 \pm 5 \%$ (8)	$31 \pm 1 \%$ (4)
	CT predicted image porosity from MIP	23.5 %	6.6 %	30.4 %
	Micro-CT segmented	17.5 %	6.9 %	28.3 %
Permeability, κ ⊥ - perpendicular to layering (z-direction) - parallel to layering (x-y plane)	Gas permeametry	⊥ 350 mD (5) 640 mD (2)	⊥ 2.77 mD (5) 7.73 mD (3)	⊥ 220* mD (2) 4600* mD (2)
	MIP	330 mD (1)	4 mD (1)	466 mD (3)
	Flow modelling	$\begin{pmatrix} 420 & 66.3 & 1.91 \\ 66.3 & 344 & 12.8 \\ 1.91 & 12.8 & 163 \end{pmatrix}$ mD	-	$\begin{pmatrix} 4517 & 5 & 38 \\ 5 & 4808 & 547 \\ 38 & 547 & 4085 \end{pmatrix}$ mD
Specific surface area, SSA (surface-to- bulk-volume)	MIP	$3.2 \mu m^{-1}$	$12.2 \mu m^{-1}$	$0.16 \mu m^{-1}$
Pore specific surface area, PSA (surface-to-pore-volume)	Micro-CT at 2.5 µm resolution size	$0.068 \mu m^{-1}$	$0.136 \mu m^{-1}$	$0.069 \mu m^{-1}$
Connectivity index	Image analysis	3.49	0.94	10
Tortuosity, τ	Flow modelling	-	-	x: 1.443 y: 1.393 z: 1.468
	Micro-CT shortest path analysis	x: 1.385 y: 1.373 z: 1.477	-	x: 1.316 y: 1.338 z: 1.394

341 Legend:

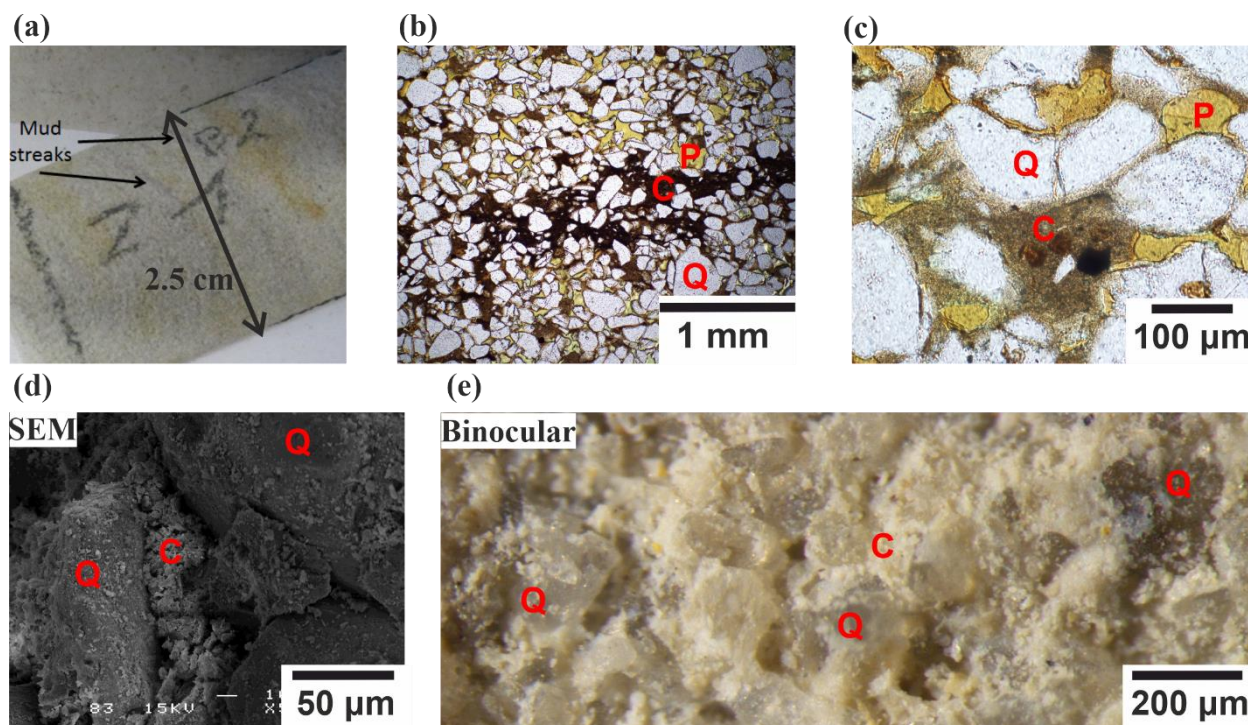
342 Numbers in parentheses related to gas porosity, gas permeability and MIP permeability, indicate the number
343 of plugs for the measurements. Other measurements and calculations were conducted on single plugs.
344 FWHM - full width at half maximum, log-normal distribution.

345

346 **Sandstone S2:** The intermediate unit layer with a thickness of ~20 cm consists of grey-green moderately
347 consolidated sandstone (Figures 1c, 4) composed of sub-rounded to rounded, very fine sand grains (~154 μm);
348 the sandstone is poorly sorted with 35 % of the particles being silt and clay (Figure 6, Table 2). Secondary silt
349 (~ 40 μm), sand (~400 μm) and clay (~1.5 μm) populations are also detected. The grains are composed of
350 quartz with minor Fe-ox coating the grains and minor quantities of heavy minerals (e.g., rutile and zirconium)
351 (Figure 4c). Clay filling the pore space was identified by XRD as a kaolinite mineral. It appears as a grain-
352 coating, meniscus-bridging, and pore-filling matrix (Figure 4b, c). Therefore, the unit layer (Figure 1c) is
353 classified as a quartz wacke sandstone (Pettijohn et al., 1987).

354 The pore space is reduced by clays deposited on coarser grains, identified mostly in laminae (Figure 4a,
355 d). However, the inter-granular connectivity of macro pores can still be recognized (Figure 4b, c). The
356 effective pore network consists of inter-granular macro pores distributed between the laminae or zones richer
357 in clay and Fe-ox. Integrating the grain size and pore throat size analysis results (Figs. 6, 7) confirms that the
358 reduction in the inter-granular pore space in S2 is due to the clay matrix, which is reflected in the poor grain
359 sorting and large variance in pore size. In the pore throat size analysis (Figure 7), only 15 % of the pore volume
360 is composed of macro pores that are larger than 10 μm . The prominent sub-micron pore mode is ~35 nm, with
361 a population containing ~45 % of the pore volume (Figure 7a). This population of pores occurs inside the clay
362 matrix. The secondary pore volume population is poorly distributed within the range of 0.8-30 μm . The
363 characteristic length (Sect. 3.2), $l_c = 12.3 \mu\text{m}$ (Figure 7b), and the pore throat length of maximal
364 conductance, $l_{max} = 8 \mu\text{m}$ (Figure A1 in Appendix A) (both lengths have large analytical uncertainties
365 resulting from uncertainty in the threshold pressure, cyan colour in Figure 7b), suggest a connectivity of macro
366 pores regardless of their small fraction within the total pore space. The porosity of S2 evaluated for 8 different
367 samples varies in the range of 14.5-23.5 % (Figure 8). From the *PTSD* (Table 1) and gas porosimetry results
368 (for a sample with a porosity of 18.6 %), micro-CT predicts an image porosity of 6.6 % at a resolution limit
369 of 2.5 μm (Table 2). The gas permeability in the z-direction was measured in 5 samples (Figure 8): in four of
370 them, the permeability ranges within 1-12 mD and increases with porosity. However, one sample had an

371 exceptionally large porosity and permeability of 23 % and 62 mD, respectively. The permeability measured
 372 for 3 samples in the x-y plane ranges within 4-12 mD, also showing ~15 % porosity (Figure 8). In addition,
 373 samples with ~15 % porosity have permeability values larger in the x-y plane (parallel to the layering) than
 374 in the z-direction (perpendicular to the layering). The permeability derived from MIP reaches 4 mD, which
 375 agrees with an average of 2.77 mD and 7.73 mD (Table 2) measured in the z-direction with a gas permeameter
 376 (excluding one exceptionally high value, Figure 8).



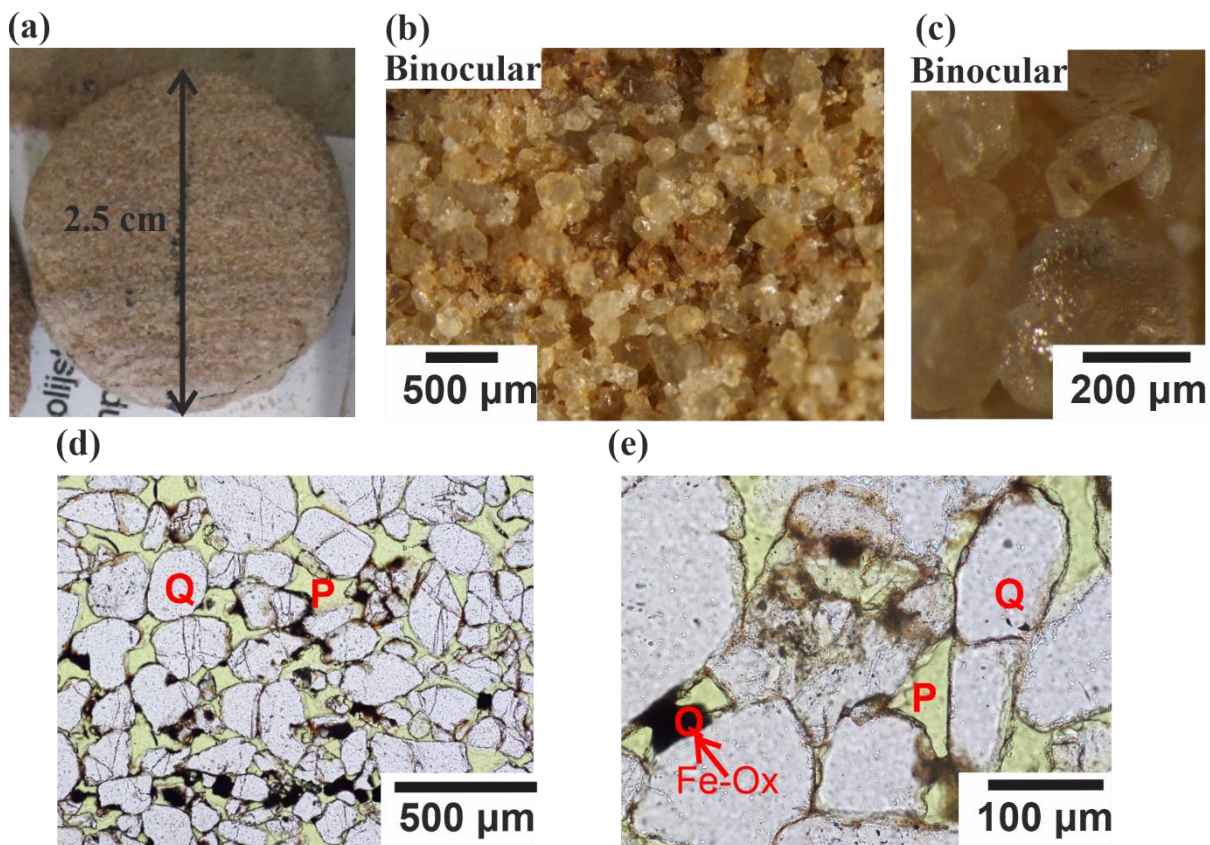
377
 378 **Figure 4.** Representative images of sandstone S2. (a) Dark stains in the rock are mud streaks, yellowish zones are due to
 379 increased Fe-Ox cement. (b) The dark laminae are richer in clays and Fe-ox. P refers to open pores, Q – to quartz, C –
 380 to clay. (c) Clay and silt accumulated as meniscus and as clay matrix. (d) Pore clogged by clay and Fe-ox. (e) Rock
 381 texture. The clay matrix is white, and quartz grains are pale grey.

382

383 **Sandstone S3:** The bottom unit layer with a thickness of ~1.5 m consists of (pale) red-purple poorly
 384 consolidated sandstone (Figure 1c) with grains covered by a secondary red patina (Figure 5). The sandstone
 385 is composed of friable to semi-consolidated, fine (~269 μm), moderately sorted sand (Table 2), where only
 386 5.6 % of particles are silt and clay (Figure 6). Secondary silt (~ 50 μm) and clay (~ 0.96 μm) populations were

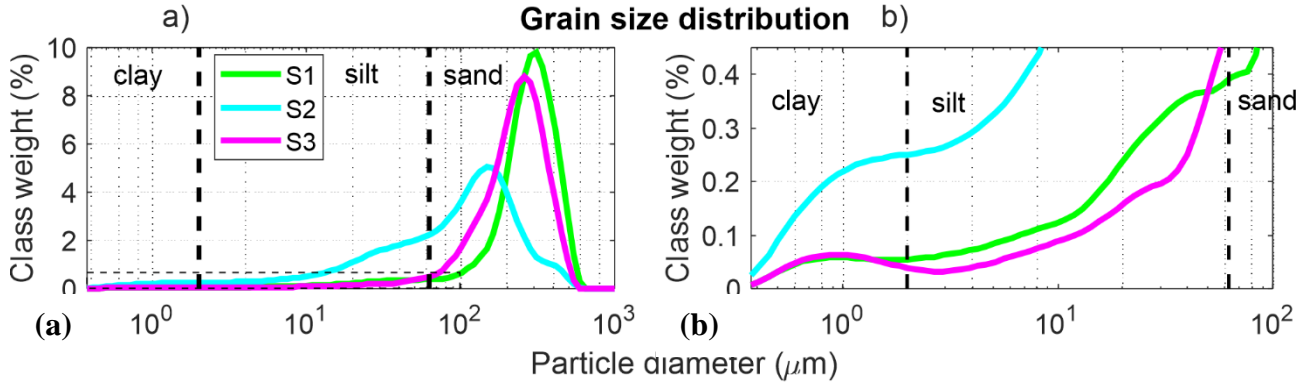
387 also detected. The sandstone consists of sub-rounded to rounded grains showing a laminated sedimentary
388 texture consisting of the cyclic alternation of relatively dark and light red bands of millimetre-scale thickness
389 (Figure 5a). The dark laminae contain slightly more Fe-ox meniscus-bridging and pore-filling cementation
390 (Figure 5b, d). Overall, this bed consists of a ferruginous quartz arenite. The grains are dominated by quartz
391 with very minor feldspar and black opaque mineral grains, perhaps Fe-ox (Figure 5d). X-ray diffraction
392 indicated quartz only. The Fe-ox coating of grains is less extensive than in other samples (Figure 5c). The
393 pore interconnectivity in this sandstone is high (Figure 5d). Heavier cementation is rarely observed (Figure
394 5d) and is organized in horizontal laminae (Figure 5a). Features including grain cracks, grain-to-grain
395 interpenetration, and pressure solution are also recognized (Figure 5e). The *PTSD* showed that 95 % of the
396 pore volume is presented by macro pores (Figure 7a), which agrees with the scarcity of fine particles. The
397 characteristic length and pore throat length of maximal conductance are $l_c = 36.9 \mu\text{m}$ (Figure 7b) and $l_{max} =$
398 $31.4 \mu\text{m}$ (Figure A1 in Appendix A), respectively.

399 The porosity measured by a gas porosimeter in the laboratory varies in the range of 30-32 % for 4
400 different samples (Figure 8). From *PTSD* and gas porosimetry (Figures 7, 8), the micro-CT-predicted image
401 porosity at a resolution limit of $2.5 \mu\text{m}$ is 30.4 % (Table 2). The permeability measured by a laboratory gas
402 permeameter averages 220 mD for 2 samples measured in the z-direction and 4600 mD for 2 samples
403 measured in the x-y plane (Figure 8), showing a ten-fold difference (discussed in Sect. 5). The permeability
404 derived from MIP reaches 466 mD (Table 2).



405
 406 Figure 5. Representative images of sandstone S3. (a) Laminae are recognized by their slightly dark and red colour. (b)
 407 General view reveals red laminae ~300 µm thick. (c) High-resolution observation of a clear grain. (d) A millimetre-scale
 408 lamina is indicated by enhanced meniscus-type Fe-ox cementation and partly by inter-granular fill. Grain surfaces are
 409 coated by thin Fe-ox. Black and orange cements represent crystallized and non-crystallized Fe-ox, respectively. Some
 410 cracked grains are observed, sporadically cemented by Fe-ox. P refers to open pores, Q – to quartz. (e) Partially dissolved
 411 grains are coated by cement.

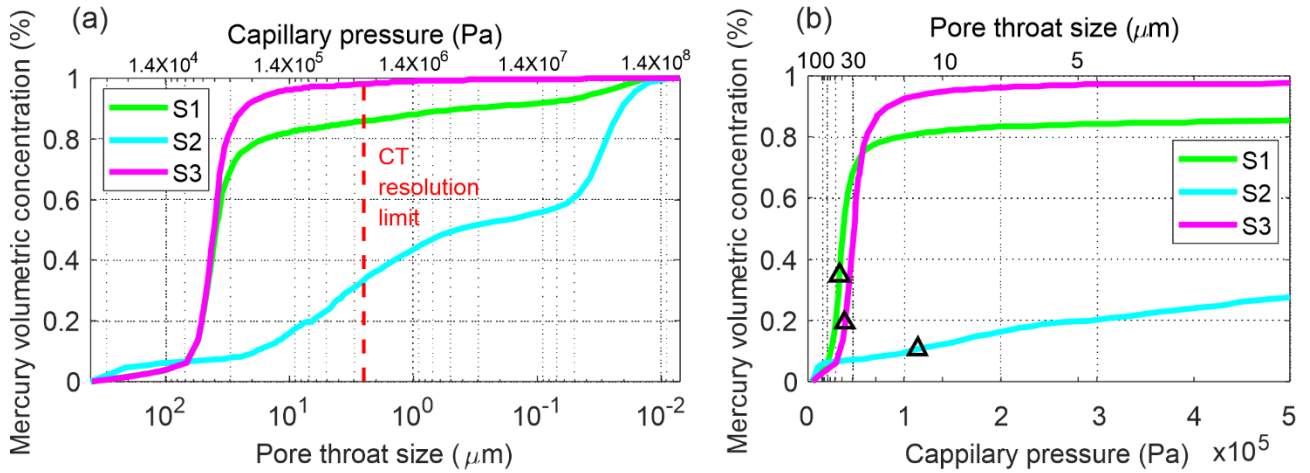
414



415

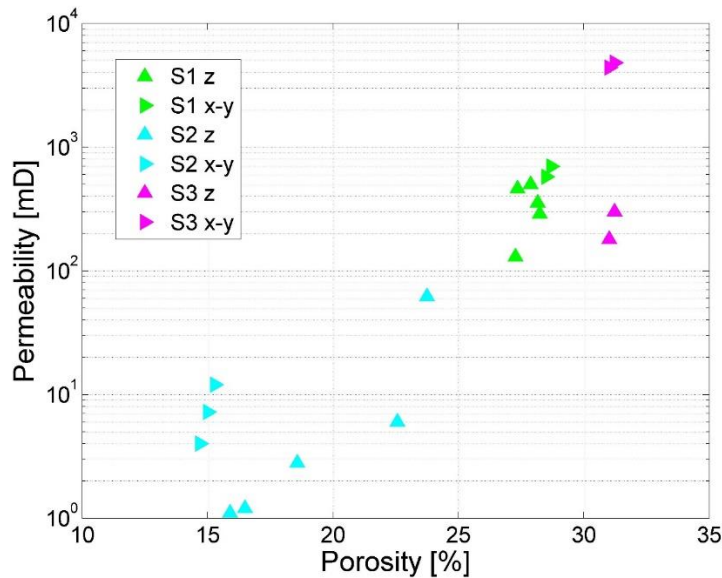
416 **Figure 6:** (a) Grain size distribution. (b) Magnified grain size distribution in the fine grain size region plotted
 417 for sandstones S1 (green), S2 (blue) and S3 (purple). S1 and S3 have a unimodal distribution and are
 418 moderately sorted with a small skewness tail. Sample S2 has a multi-modal distribution and is poorly sorted.

419



420 **Figure 7:** Cumulative pore throat sizes of the studied sandstones. (a) Capillary pressure on a logarithmic
 421 scale. The resolution limit of the micro-CT imaging indicates the fraction of the pore space that could be
 422 resolved. (b) Capillary pressure on a linear scale. The triangles indicate the characteristic length, l_c .

423



424

425 **Figure 8:** Results of porosity-permeability lab measurements. The permeability of the samples was measured
426 in directions perpendicular to the bedding (z-direction) and parallel to the bedding (x-y plane).

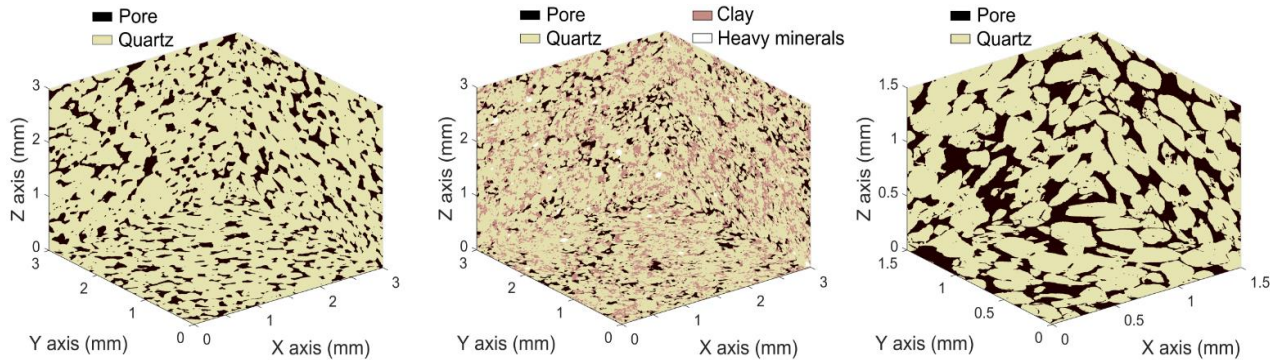
427 Overall, the relative decrease in l_{max} with respect to l_c is greater for the layers containing more fines
428 (Table 2).

429 Additionally, pore surface roughness may be evaluated from the specific surface area (SSA) measured
430 by MIP (Table 2). A larger SSA implies a rougher surface (e.g., Tatomir et al., 2016). The SSAs for S1 and S2
431 ($3.2 \mu\text{m}^{-1}$ and $12.2 \mu\text{m}^{-1}$, respectively) are similar to those given in the literature for sandstones of similar
432 properties (e.g., Cerepi et al., 2002). The SSA of S2 is higher because of its high silt and clay content of 34.3
433 %, which is only 7.4 % for S1 (Figure 6a). The SSA of S3 (where silt and clay constitute only 5.6 %, including
434 the Fe-ox rim coating) is only $0.16 \mu\text{m}^{-1}$, which is 20 times smaller than that of S1 (Table 2). The difference
435 in SSAs between S1 and S3, which are similar in their grain and pore throat size distributions (Figs. 6, 7), is a
436 result of S1 having a higher Fe-Ox grain coating than S3 (compare Figures 3d and 5c).

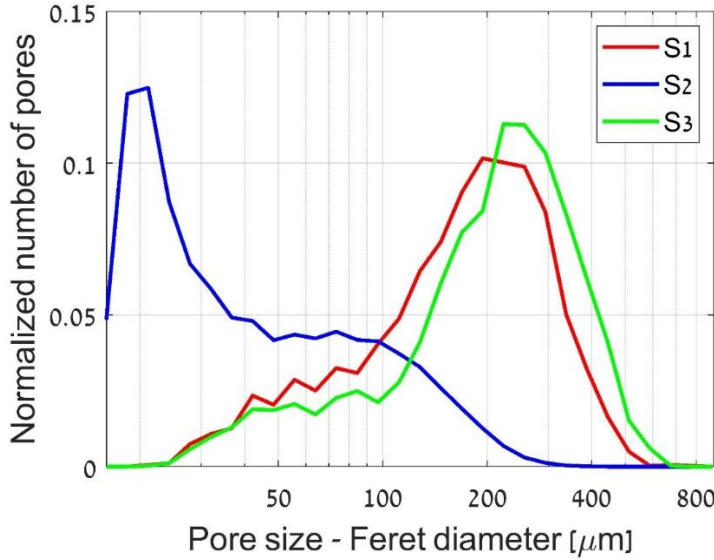
437 In summary, although the S1 pore network has larger pore throats, it also has greater grain roughness
 438 and lower connectivity than S3. These two properties dominate and generate a smaller permeability for S1
 439 than for S3 (Table 2).

440 4.2. Image analysis

441 Visualized segmented sub-volumes of samples S1, S2, and S3, depicting quartz, pores, clay and heavy
 442 minerals, are presented in Figure 9. The main pore size population in PSD of S1 is at $\sim 100\text{-}500\text{ }\mu\text{m}$ range with
 443 majority at $\sim 194\text{ }\mu\text{m}$ (Figure 10). A smaller population of pores of $\sim 30\text{-}100\text{ }\mu\text{m}$ was identified as well, which
 444 may refer to (Mode 1) pore throat size derived from the MIP experiment (Table 2). Image resolution of $2.5\text{ }\mu\text{m}$
 445 limited the analysis. The pore specific surface area (*PSA*) calculated from micro-CT images is
 446 $0.068\text{ }\mu\text{m}^{-1}$. The tortuosity, measured from the whole CT image, indicates similar values in the x- and y-
 447 directions of 1.37 and 1.38, respectively, whereas in the z-direction, the tortuosity is 1.48 (Table 2). As many
 448 paths were considered, this difference indicates the textural features that appear in horizontal plane (Figure
 449 3a).



450 **Figure 9:** Visualized in these pictures sub-volumes of segmented CT samples of (a) S1, (b) S2, (c) S3. S1 and
 451 S2 in this visualization have volumes 3^3 mm^3 scanned with $5\text{ }\mu\text{m}$ voxel size resolution, S3 has volume 1.5^3 mm^3
 452 scanned with $2.5\text{ }\mu\text{m}$ voxel size.



454

455 **Figure 10:** Statistics of the pore sizes calculated by image analysis for three sandstone samples: S1, S2, and
 456 S3. Number of pores analysed: S1 – 3500, S2 – 45000, S3 – 3500. The CT data sets used for this analysis had
 457 2.5 μm voxel size resolution to capture grain and pore shapes better, compared to those at resolution of 5 μm .

458 For S2 (Figure 9), the main pore size population is in the ~15-50 μm range (Figure 10), with majority
 459 at ~21 μm . This may refer to the pore throat size derived from MIP. However, smaller pore throat sizes which
 460 were derived from the MIP (mode peak is at ~3.5 μm) could not be visualized due to the limited resolution of
 461 the image (2.5 μm), and because of high uncertainty associated with size of pores smaller than 10 μm (four
 462 voxels). Accordingly, they were excluded from the PSD evaluation (Figure 10). A large pore population is
 463 also recognized at ~100 μm (Figure 10), which corresponds to the pore size scale recognized from the
 464 petrography (Figure 4), MIP (Figure 7) and CT image (Figure 9). The pore specific surface area (PSA)
 465 calculated from micro-CT images is $0.136 \mu\text{m}^{-1}$ (Table 2), which is twice as large as the PSA of S1.

466 For S3 (Figure 9), the main pore size population is in the ~100-500 μm range (Figure 10), with majority
 467 at ~223 μm . The geometry-based tortuosity values measured from the whole CT image with multiple paths is
 468 1.32, 1.34 and 1.39 in the x-, y- and z-directions, respectively. The tortuosity is lower for S3 than for S1 in all
 469 directions, which is a direct result of the smaller amount of cement in the pore throats. The PSA of S3 is
 470 $0.069 \mu\text{m}^{-1}$, which is similar to that of S1.

471 4.3 REV Analysis

472 4.3.1. Quartz arenite sandstones (S1 and S3)

473 One-dimensional profiles of porosity of S1 (Figure 11(a-c)) were evaluated by averaging the pore
474 voxels over each slice in sequential slices in three orthogonal directions (hereafter referred as slice-by-slice
475 porosity). The investigated domain had a volume of $6.8 \times 6.9 \times 9.2 \text{ mm}^3$ scanned with a voxel size of $5 \mu\text{m}$
476 (suitable for imaging pore throats that effectively contribute to the flow in S1, Table 2). The slice-by-slice
477 porosity distinguishes the z-direction as having an exceptional behaviour, with variance in porosity
478 fluctuations being four times larger than that in x- and y- directions (i.e., 0.98 in z- direction, compared to 0.17
479 and 0.16 in the x- and y- directions, respectively). Porosity fluctuates with peak to trough length of $\sim 0.1 \text{ mm}$
480 in x- and y- directions that could refer to an average pore cross-section over the slice, and thus being attributed
481 to grain packing. In z- direction an additional larger scale wavelength of $\sim 3.5 \text{ mm}$ is observed, where peaks
482 and troughs could refer to higher and lower porosity layers, respectively, thus being attributed to depositional
483 processes.

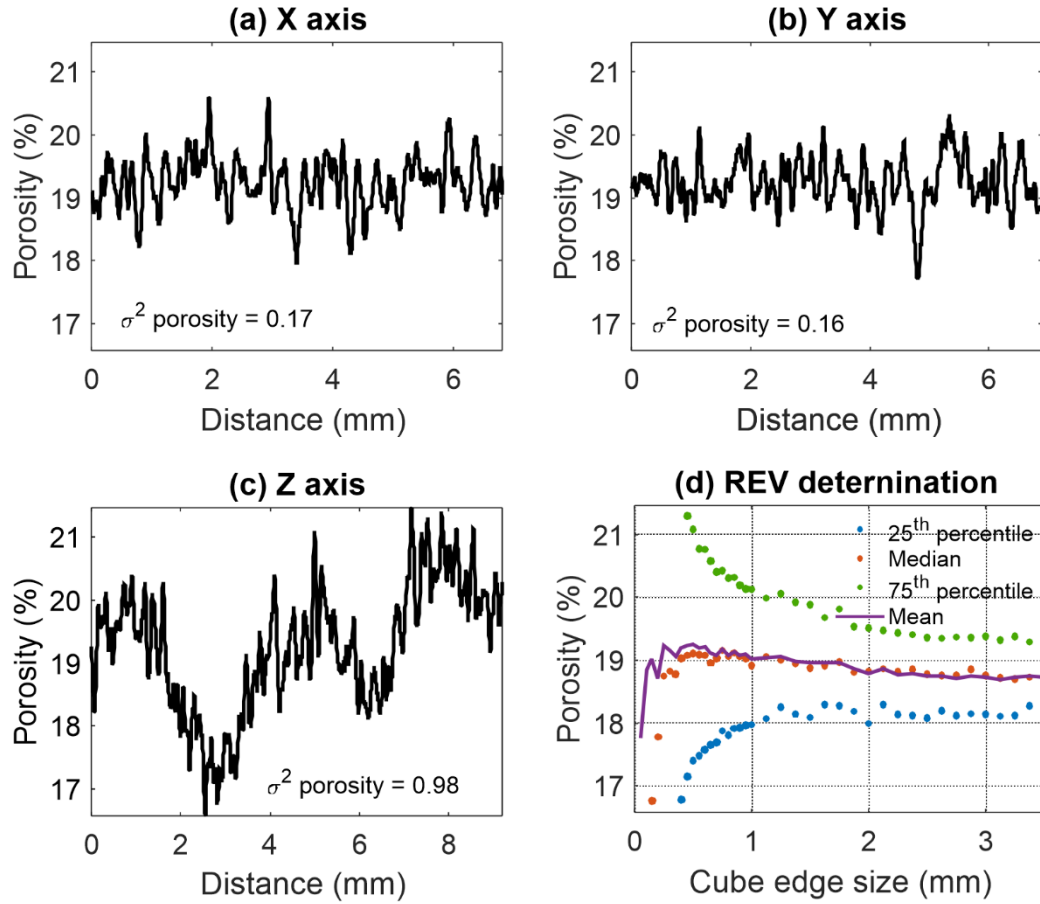


Figure 11: Determination of REV in S1. a) One-dimensional porosity profile of S1 slices evaluated in a) x-direction, b) y-direction and c) z-direction. (d) Classic REV analysis. Investigated volume size is $6.8 \times 6.9 \times 9.2 \text{ mm}^3$.

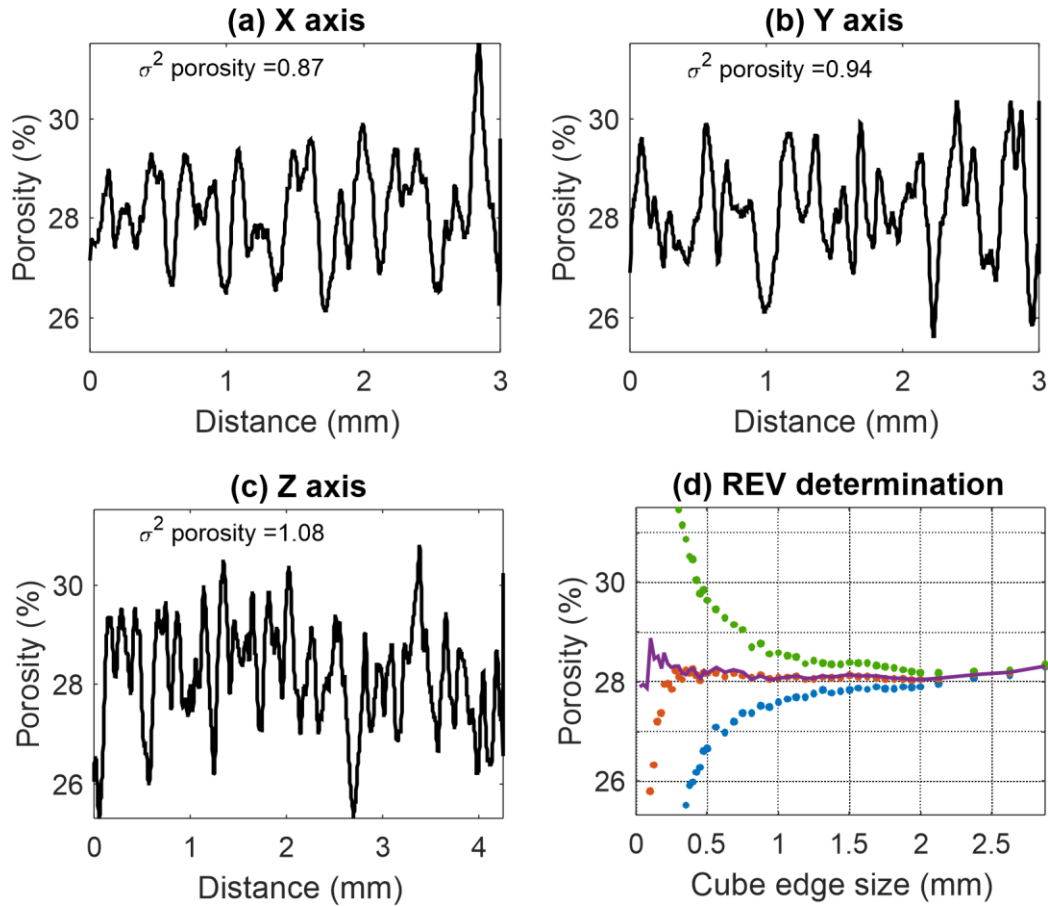
Alternatively, the REV size was estimated as $\sim 2.5 \text{ mm}$ (Figures 11d) by classic REV analysis, where the mean, median, 25th and 75th percentile porosity changes decline. Considering these results (Figure 11), we decided to use a segmented specimen cube with a maximal available edge length of $2950 \mu\text{m}$, scanned with a higher resolution of $2.5 \mu\text{m}$ (to preserve the grain surface geometry and a consistency between S1 and S3 samples) for flow simulations.

One-dimensional profiles of slice-by-slice porosity were evaluated in sequential slices in the orthogonal directions of S3 with a maximal segmented volume of $3 \times 3 \times 4.2 \text{ mm}^3$ scanned with a voxel size of $2.5 \mu\text{m}$

495 (Figures 12a-c). Porosity fluctuates in all directions with peak to trough distance of ~ 0.1 mm that could refer
 496 to an average pore cross-section over the slice, as clarified for S1. The variance is similar in all directions
 497 (0.87, 0.94, 1.08, correspondingly) that implies a homogenous sample. REV with an edge length of $875 \mu\text{m}$
 498 was estimated by classic analysis (Figure 12d), which was used for the flow simulation in S3.

499

500

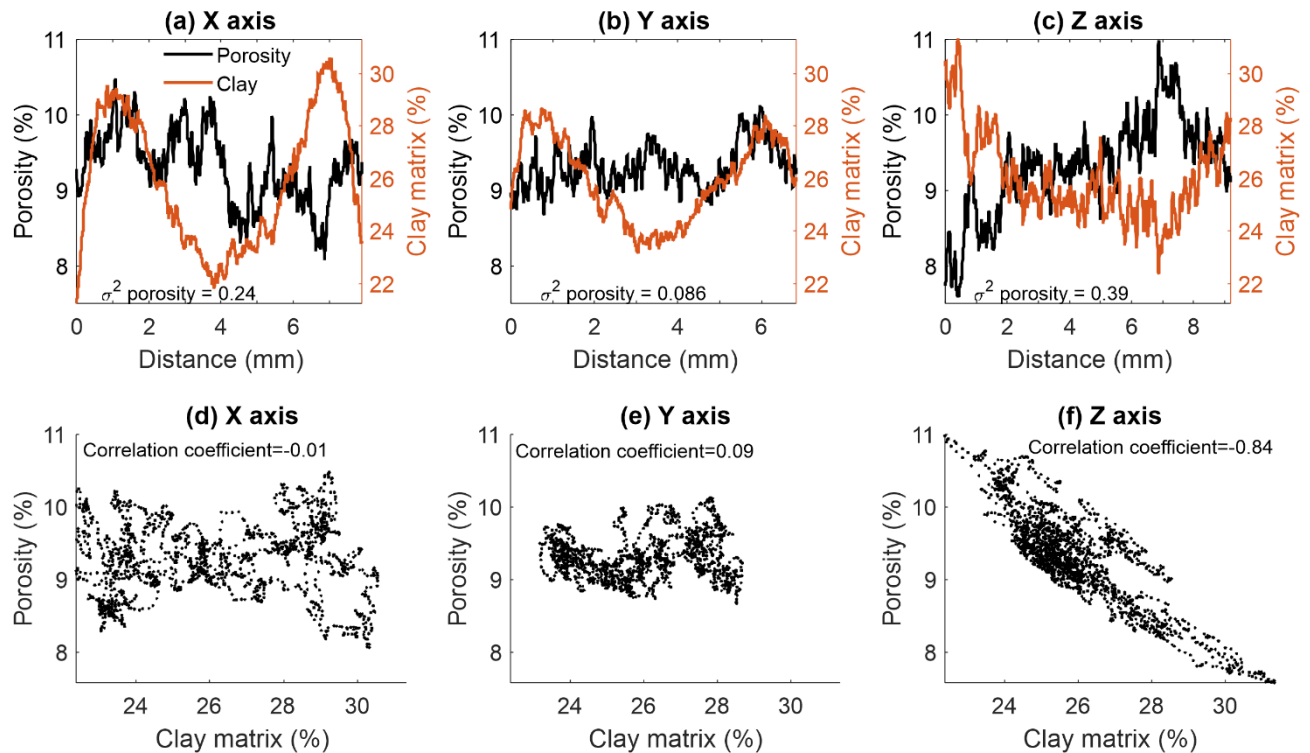


501

502 **Figure 12:** Determination of REV in S3. a) One-dimensional porosity profile of S3 slices evaluated in a) x-
 503 direction, b) y-direction and c) z-direction. (d) Classic REV analysis. Investigated volume size is $3 \times 3 \times 4.2$
 504 mm^3 .

505 **4.3.2. Quartz wacke sandstone (S2)**

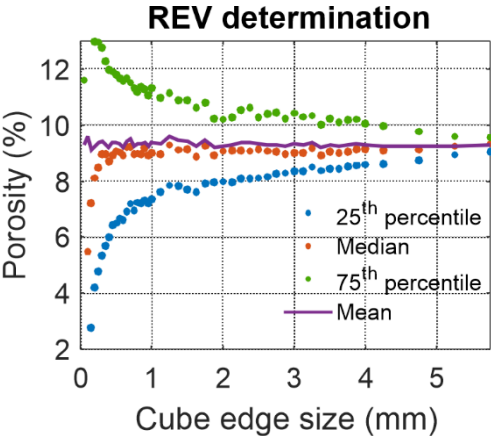
506 Sample S2 is more heterogeneous than S1 and S3 because of the deposition of clay in a patchy
507 distribution. The sample is visualized in Figure 9b with quartz grains (yellow), pore volume (black), clay
508 matrix (brown) and heavy minerals (white). In Figure 13a-c, the porosity of sequential slices in the orthogonal
509 directions is shown together with clay matrix content, evaluated in segmented volume of $7.9 \times 6.8 \times 9.2 \text{ mm}^3$
510 size scanned with a voxel size of $5 \mu\text{m}$. In z-direction a clear trend in porosity is observed, which has a negative
511 correlation with the clay content (Figure 13f), whereas in the horizontal (x-y) plane there is no clear correlation
512 (Figure 13d-e). This correlation in z- direction implies that the porosity is controlled by depositional processes.
513 However, the similar large-scale wavy structures of the clay content in x- and y- directions (Figures 13a, b)
514 may refer to errors originated from the scanning and inversion in the CT acquisition, as x- and y-coordinates
515 are associated with the side boundaries of the cylindrical sample



517 **Figure 13:** Correlation between porosity and clay. Porosity and clay profiles (left and right y-axes,
518 correspondingly) in slices of S2 evaluated in (a) x-direction, (b) y-direction (c) z-direction. Scatterplots of clay

519 content and porosity in S2 in (d) x-direction, (e) y-direction, (f) z-direction.) Investigated maximal segmented
520 volume size is $7.9 \times 6.8 \times 9.2 \text{ mm}^3$ (see text for more detail).

521



522

523 *Figure 14: Classic REV analysis of S2. Investigated volume size is $7.9 \times 6.8 \times 9.2 \text{ mm}^3$.*

524 Classic REV evaluation (Figure 14d) may indicate a cube edge size of $\sim 3 \text{ mm}$. However, the porosity
525 trend in z-direction (Figure 13c) in the volume under investigation, implies that no REV can be found in S2
526 sample. As a result, flow modelling could not be conducted in sample S2.

527 **4.4. Flow modelling at the pore scale**

528 Fluid flow was modelled at the pore scale in two different micro-CT-scanned geometries: 1) a full cube
529 of sample S1, and 2) sample S3 within its REV dimensions (Table 3), imaged with $2.5 \text{ }\mu\text{m}$ voxel size.
530 Modelling of the 3D geometry of sample S2 was not performed due to its non-stationarity, which did not allow
531 finding the REV in the investigated domain.

532 **Table 3.** *Porosity losses in S1 and S3 over the course of applying the extended computational workflow (Figure*
533 *2).*

Sample	Sample size (mean mesh edge size) [μm]	CT segmented image porosity (%)	Connected porosity (%)	Mesh porosity (%)	Gas porosity (%)
S1 (entire sample, 1180 voxels)	2950 (14)	17.5	15.6	13.6	28
S3 (REV, 350 voxels)	875 (5)	28.3	27.9	25.9	31

534

535 The porosity of the meshed domain of sample S1 is 13.6 % (in contrast to 17.5 % in the segmented
 536 image, Table 3), and the mesh edge length is 14 μm along the pore walls. The observed porosity loss results
 537 from disconnecting narrow pore throats from the connected cluster imaged with a 2.5 μm voxel size due to
 538 the use of a 14 μm mesh size (the lowest possible for our computational needs). A maximum Reynolds number
 539 of $Re = 0.084$ was used to guarantee the simulation in a creeping flow regime.

540 The symmetrized permeability tensor, $\bar{\kappa}$ (Eq.5), was obtained as follows (Table 2):

$$541 \quad \bar{\kappa}_{sym} = \begin{pmatrix} 420 & 66.3 & 1.91 \\ 66.3 & 344 & 12.8 \\ 1.91 & 12.8 & 163 \end{pmatrix} \quad (6)$$

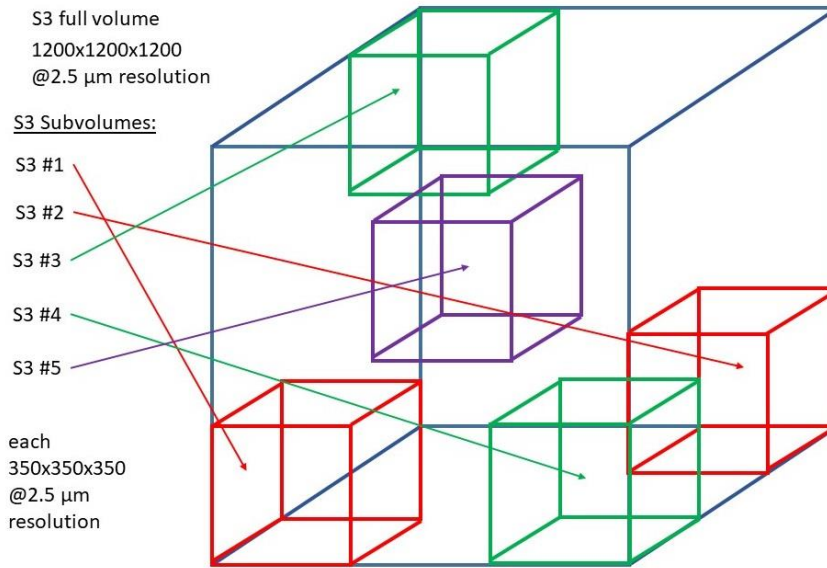
542

543 The permeability tensor is anisotropic, with κ_{zz} being more than twice smaller than κ_{xx} and κ_{yy} . This
 544 result is in agreement with the appearance of horizontal banding with higher cementation (Figure 3a).

545 The porosity of the meshed domain of sample S3 is 25.9 % (in contrast to 28.3 % in the segmented
 546 image, Table 3), and the mesh edge length is 5 μm along the pore walls. A maximum Reynolds number of
 547 $Re = 0.22$ was used to guarantee the simulation in a creeping flow regime. The symmetrized permeability
 548 tensor is close to isotropic (Table 2):

$$549 \quad \bar{\kappa}_{sym} = \begin{pmatrix} 4517 & 5 & 38 \\ 5 & 4808 & 547 \\ 38 & 547 & 4085 \end{pmatrix} \quad (7)$$

550 Additional permeability tensor simulations on equivalently REV sized segmented sub-volumes of S3
 551 and on the full S3 (Figure 15, cube volume of $3 \times 3 \times 3 \text{ mm}^3$) have been performed with GeoDict toolbox, to
 552 ensure consistency of the estimated REV size. Sub-volumes locations are presented. Symmetrized
 553 permeability tensors simulated in these domains (Figure 16) are close to the former one (Eq. 7) being also
 554 nearly isotropic.



555

556 **Figure 15:** Selection of the sub-volumes in the S3 CT dataset, for additional permeability tensor simulations.

557 Each sub-volume has a size of 350 voxels cubed, while full volume is of 1200 voxels cubed size.

558

S3_full	4247	98	117	avg. k: ~4500 mD $\phi = 26.88 \%$	S3_#3	5032	5	6	avg. k: ~4799 mD $\phi = 27.33 \%$
	98	4820	483			5	4143	10	
	117	483	4432			6	10	5223	
S3_#1	5485	125	4	avg. k: ~5290 mD $\phi = 27.47 \%$	S3_#4	4601	4	4	avg. k: ~3915 mD $\phi = 26.75 \%$
	125	5882	2			4	3799	5	
	4	2	4504			4	5	3344	
S3_#2	4392	122	4	avg. k: ~3754 mD $\phi = 25.99 \%$	S3_#5	4397	10	70	avg. k: ~4027 mD $\phi = 27.53 \%$
	122	3510	185			10	3825	6	
	4	185	3359			70	6	3858	

In sub-samples: avg. k: 4381 mD / median k: 4522 mD

Figure 16: Permeability tensor simulation results and evaluated 3D image porosity data for the sub-volumes and full sample S3 specified in Figure 15.

The tortuosity of S3 computed from particle tracing in the x-, y-, and z- directions is 1.44, 1.39 and 1.47, correspondingly (Table 2). The largest value is observed in the z-direction, which is in agreement with the lowest permeability in the z-direction.

5. Discussion

5.1. Validation of permeability by micro- and macro-scale rock descriptors

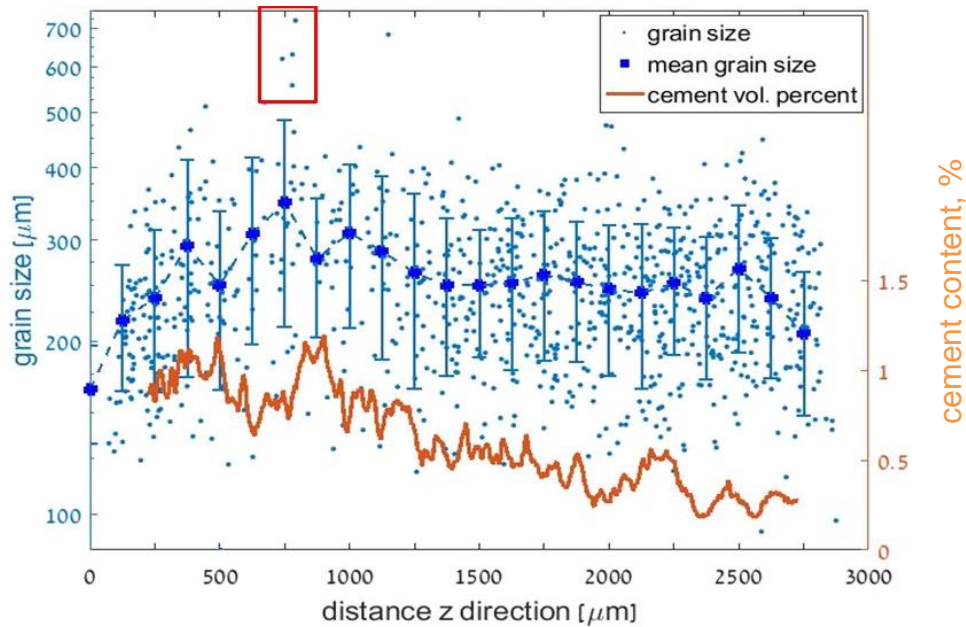
Each of the evaluated micro- and macro-scale rock descriptors supplies a qualitative information about the sample permeability (Tables 2-3), which is used to validate the multi-methodological approach presented in this paper. Specifically, the increasing mercury effective saturation with increasing pressure shows a similar pore throat size distribution curve slope for sandstone samples S1 and S3 in the macro-pore throat range (Figure 7), suggesting that these samples have similar structural connectivity. However, S1 has a smaller imaged volume fraction of pore space available for fluid flow that is controlled by macro pore throats (i.e., 81

583 % in S1 vs. 93 % in S3, Figure 7) due to its higher contents of silt, clay, and Fe-ox cement. The intermediate
584 layer (S2) with 19 % porosity comprises more fines, which form a clay matrix (Table 2) due to poor grain
585 sorting and smaller mechanical resistance of clay to pressure under the burial conditions. Only ~15 % of the
586 pore volume fraction in S2 is controlled by bottle-neck macro pore throats (Figure 7). However, the
587 characteristic length of S2, 12.3 μm (Table 2), indicates that macro-pore connectivity is still possible even
588 when the pore space consists mainly of sub-macro-scale porosity. This 0.15 volume fraction is in agreement
589 with Harter (2005), who estimated a volume fraction threshold of 0.13 for correlated yet random 3D fields
590 required for full interconnectivity.

591 The value of the connectivity index of S3 (10) evaluated from CT data is approximately three times higher
592 than that of S1 (3.49), while both rocks are defined as moderately sorted sandstones (Table 2). This difference
593 is due to S1 having a smaller number of inequivalent loops within the imaged pore network than S3, leading
594 to smaller Euler characteristics (see Supplementary material for more detail). Inequivalent loops are positively
595 correlated with pore throats; their number is affected by the resolution of the CT image and by the partial
596 volume effect at grain surfaces (Cnudde and Boone, 2013; Kerckhofs et al., 2008), where some voxels could
597 be identified as grains and thus “clog” the small pore throats. Artefact porosity loss is apparent for S1, where
598 the IP is 17.5 % (in contrast to the CT porosity of 23.5 % predicted from MIP, Table 2). The connectivity
599 index of S2 (0.94, Table 2) is lower than those of both S1 and S3 because of the clay matrix, which clogs
600 pores with sizes below the image resolution. The effect of the partial volume effect on the image connectivity
601 and on the preservation of small features was reviewed by Schlüter et al. (2014).

602 A correlation was found between the grain size and the amount of Fe-ox cement in S1 evaluated at each
603 slice along the z-direction (from the image analysis, Figure 17). Exceptionally large grains are detected
604 (indicated by the red rectangle) near the cemented region at ~750 μm . Large grains and a relatively high
605 amount of cement can also be observed in the S1 thin section (Figure 3b). Large grains cause large pores and
606 generate relatively permeable horizons through which water flow and solute transport can become focused
607 (McKay et al., 1995; Clavaud et al., 2008), supplying iron solutes. We suggest that a vadose zone was formed
608 after flooding events, where the water flow mechanism could have changed from gravity dominated to
609 capillary dominated. Water then flowed due to capillary forces along grain surfaces towards regions with
610 larger surface areas, and iron solutes precipitated in a reaction with oxygen available in the partly saturated
611 zone. We suggest that with time, this cementation mechanism caused a decrease in the pore throat size near

612 the preferential path, while the preferential path with a low surface area remained open, eventually generating
 613 the observed anisotropic flow pattern.



614

615 **Figure 17.** Grain size scattering and Fe-ox cement content in sandstone S1 in slices along the z-direction. The
 616 red rectangle emphasizes very large grains that were detected.

617 In this respect, permeability anisotropy in sandstones at a small scale is usually attributed to the shape or
 618 preferential orientation of grains and pores (e.g., Sato et al., 2019) and to a heterogeneous distribution of
 619 cementing material at grain contacts (Louis et al., 2005). Clay-free and cement-free layers in S1 thus constitute
 620 the main avenues for flow in the parallel direction, shown by variation in porosity in z-direction (Fig. 11c)
 621 that is correlated with anisotropic permeability tensor (Eq. 6). At a larger scale, a higher degree of permeability
 622 anisotropy is usually associated with the presence of localized beds, foliation, and compaction bands that
 623 constitute barriers to flow in the perpendicular direction (see Halisch et al., 2009; Clavaud et al., 2008 and
 624 references therein).

625 Flow modelling in the specified REV of S1 shows anisotropy (Table 2) and an average permeability value
 626 of 310 mD that is close to that derived from MIP (330 mD). However, the average permeability is lower than

627 the average experimental gas permeability (~543 mD); this difference should be related to the loss of porosity
628 due to limitations on the CT resolution, image processing and meshing (Table 3, see Sect. 5.2 for more details).

629 In contrast, flow modelling and upscaling to the macro scale indicate an isotropic S3 sample (Eq.7).
630 However, the modelled permeability (~4500 mD) is ten times higher than the MIP-derived permeability (~466
631 mD, Table 2). Gas permeability measurements indicate anisotropy, yielding permeabilities of ~4600 mD in
632 the x-y plane and ~220 mD in the z-direction (with an anisotropy ratio of ~20, defined here as $\kappa_{\parallel}/\kappa_{\perp}$, e.g., Tiab
633 and Donaldson, 2004). For comparison, the values of this ratio obtained from experimental permeability
634 measurements were ~1.2 for Bentheim sandstone (Louis et al., 2005), ~1.7-2.5 for a sandstone within the
635 Cretaceous Virgelle Member, Alberta, Canada (Meyer and Krause, 2001), and ~8.5 for Berea sandstone (Sato
636 et al., 2019). However, in our laboratory measurements conducted parallel to the layering (in the x-y plane),
637 poorly cemented grains in S3 could dislocate from the weakly consolidated sample due to the application of a
638 pressure gradient. This could have resulted in a higher measured gas flux and thus a higher permeability
639 parallel to the layering, yielding a high anisotropy.

640 Alternatively, the disagreement between the laboratory-determined permeability perpendicular to the
641 layering, κ_{\perp} , and the isotropic permeability obtained from the flow modelling (Table 2, Eq.7) may also stem
642 from the small dimension of the modelled REV domain (cube edge length of ~0.875 mm), which may not
643 have included the additional textural features (e.g., Figure 5d) that constrain fluid flow on a larger scale of the
644 lab sample of S3 (2.5 cm in diameter and 5-7 cm in length).

645 However, the consistency of the REV size in S3 by the additional permeability simulations on
646 equivalently REV sized segmented sub-volumes and on the entire sample (Figures 15, 16), is confirmed by
647 yielding nearly isotropic permeability tensors that are also in a good agreement with previously simulated
648 permeability tensor in the REV (Eq.7). The average permeability derived from all REV-sized sub-volumes is
649 ~4381 mD, compared to the average permeability of ~4500 mD simulated over the entire S3 geometry. This,
650 again, is in a good accordance with the gas permeability of S3 measured parallel to the layering (~4600 mD,
651 Table 2). These additional simulation results (Figure 16), strengthen our conclusion that those may not have
652 included the textural features that constrain fluid flow on a larger scale of the sample S3 tested by the
653 laboratory experiments. Similarly, the differences with the permeability estimated by MIP seem to originate
654 from the same reason.

655 For sample S2, REV and slice-by-slice porosity analysis indicated an REV size larger than the
656 investigated sample size (Figure 13c, 14). For this reason, the analytical programme formulated in our study
657 cannot entirely be applied to S2 due to the impossibility of determining a reliable REV and hence conducting
658 pore-scale flow modelling. As a result, although sample S2 represents a common sandstone, it is very
659 heterogeneous in nature, and a sample larger than at least 9 mm (which is a maximal length in z-direction of
660 the tested domain (Figure 13c)) is required to capture its REV. The MIP-derived permeability is 4 mD; this
661 low permeability is due to a clay-rich matrix that encloses substantial void space (Hurst and Nadeau, 1995;
662 Neuzil, 2019). The gas permeability of the quartz wacke layer (S2, ~4.6 mD on average) is approximately two
663 orders of magnitude lower than that of the quartz arenite layers (S1 and S3, Table 2). The permeability
664 anisotropy ratio of S2 is ~2.8. The high inverse correlation between the porosity and clay matrix content
665 enhanced in the z-direction (Figures 13c,f) suggests that the clay matrix pattern appears as horizontal layering,
666 thus generating the observed anisotropy.

667 Finally, non-marine sandstones of Lower Cretaceous age (as well as sandstones in general), feature a
668 big complexity and variability in their characteristics, as immediately seen even from a comparison of our
669 samples S1, S2, S3 from the same outcrop (Table 2). For instance, low porosity of Wealden quartz arenite
670 sandstones from Weald Basin within Ashdown and Wadhurst Clay Fms. in southeast England, ranges between
671 6.3 % and 13.2 %, while permeability between 0.4 mD and 11.9 mD (Akinlotan, 2016), suggested to be
672 controlled mainly by grain sizes, grain shapes, and sorting that are directly linked to their depositional
673 environment. Average porosities of 3.06 % and 0.19 % were evaluated in medium and fine grained
674 tight gas sandstones, correspondingly, from Lower Cretaceous Dengloulou Fm. in the Songliao Basin,
675 China (Zhang et al., 2019). Alternatively, a secondary porosity of 4 % to 22 % was generated by
676 acidic fluids acting in the compactional regime, destructing a high primary porosity in sandstone of
677 Lower Cretaceous Shurijeh Fm. in the eastern Kopet-Dagh Basin in NE Iran (Moussavi-Harami and
678 Brenner, 1993). Significant average porosity and permeability of 20 % and 3700 mD, respectively,
679 were quantified in the Masila Block, Upper Qishn Fm. of the Lower Cretaceous Age, Republic of
680 Yemen (Harding et al., 2002). Multi-methodological approach suggested in this study is applicable
681 to all those sandstones with broad ranges of their textural, topological and mineralogical
682 characteristics and should lead to their accurate petrophysical characterization.

5.2. Upscaling permeability: accuracy of the extended computational workflow

The extended computational workflow (Figure 2) serves as the main tool in this study for upscaling permeability from the pore-scale velocity field. The accuracy of each step in the workflow affects the ultimate result.

Following the steps of the workflow, a micro-CT image resolution of 2.5 μm limits the reliability of the representation of the porous medium and defines the lower pore identification limit using this method. As an example of this limitation, the *SSA* (bulk specific surface area) calculated by MIP is larger than the *PSA* (pore specific surface area) calculated by micro-CT image analysis in all the samples (Table 2), although the pore volume is always smaller than the bulk volume. The *PSA* from micro-CT is limited by the image resolution and therefore does not consider relatively small pores with large surfaces. The *PSAs* of S1 and S3 are similar, but the *SSA* (from MIP) of S1 is 20 times larger than that of S3 because S1 has a larger surface area at small pores created mainly by Fe-ox cement (compare Figure 3c-f for S1 to Figure 5c for S3). In contrast to *SSA*, *PSA* in S2 is only twice as large as that of S1 due to the presence of clay and clay matrix with large surface areas.

Image processing and segmentation were applied in this study to recover the image geometry, which was blurred by noise or affected by the partial volume effect (see Sect. 3). Then, the loss of pore space due to the resolution limits was estimated in this study from the amount of mercury filling the pores with diameters equal to the resolution limit (Figure 7a). After segmentation, sample S1 had a segmented image porosity of 17.5 % and a CT predicted porosity of 23.5 % from MIP (Tables 2, 3). Therefore, the difference in porosities generated by the partial volume effect in the image processing scheme (e.g., Cnudde and Boone, 2013) is a significant component of error, especially for small structures, such as pores with a large surface area-to-volume ratio. In contrast, the image porosity of S3 after segmentation was 28.3 %, which is close to the porosity of 30.4 % estimated from MIP (Tables 2, 3). This is a result of the very small degree of cementation and the absence of Fe-ox flakes in the majority of the sample pores, leading to the small contribution of the partial volume

709 effect. In comparison, a fine-grained and well-sorted Lower Cretaceous Fm. sandstone from Heletz
710 Field (e.g., Figure 1a) (Tatomir et al., 2016) comprising clay and calcite, had MIP and micro-CT
711 porosities of 26.7 % and 20.9 %, respectively.

712 An additional source of inaccuracy is the use of a porosity-based REV for permeability approximations.
713 Mostaghimi et al. (2012) showed that for CT images of sandpacks (homogenous samples), the porosity-based
714 REV had an edge length of 0.5 mm, whereas the permeability-based REV was twice as large. Moreover, the
715 porosity- and permeability- based REV values in images of crushed bead packs derived by Zhang et al. (2000) had
716 edge lengths of 1.71 and 2.57 mm, respectively. According to Mostaghimi et al. (2012), larger REV values for
717 permeability rely on contributions from the tortuosity and connectivity of pore spaces, whereas the larger REV
718 values of Zhang et al. (2000) might be related to the heterogeneity of the sample.

719 This discrepancy indicates a larger REV for a rock property evaluated using physics-based simulations
720 than for those estimated using morphology-based methods (Saxena et al., 2018 and references therein).
721 Furthermore, implementing the classic REV determination methodology (e.g., Callow et al., 2020) using very
722 small search sub-volumes is not in agreement with capturing a sufficient structural complexity (Saxena et al.,
723 2018).

724 Flow simulations performed in sub-volumes and full sample of S3 (Figures 15, 16) support this
725 conclusion. Small dimensions of the evaluated REV (~ 0.875 mm) of homogeneous S3 ensure efficient
726 calculations. Both, porosity and permeability demonstrate a good agreement (Table 2, Figure 16), thus
727 confirming a representativeness of the estimated REV and a continuity of these characteristics over the chosen
728 sample. However, the differences in porosity between the sub-samples and the full sample are smaller than the
729 corresponding differences in permeability (Figure 16), as anticipated from the porosity-based REV derivation
730 discussed above.

731 An additional verification of the REV size for flow simulations in S3 follows the approach given by
732 Saxena et al. (2018). They demonstrated that for homogeneous sandstones, the smallest pore throats can be
733 accurately resolved at $N_l > 10$, where $N_l = D_D/\Delta x$ is a ratio of the pore throat size corresponding to mercury
734 entry pressure, D_D , and of the voxel size, Δx . N_l controls the lower bound on permeability that can be reliably
735 calculated using a digital rock image, to capture sufficient structural complexity of rock microstructure which
736 affects flow, attributed to D_D visualized using Δx . For our sub-volumes of sample S3 imaged with $\Delta x = 2.5$
737 μm resolution, and $D_D = 35 \mu\text{m}$ (Table 2), $N_l = 14 > 10$. In addition, there is a requirement for the minimal

738 REV size for representativeness for permeability calculation, $N_{REV} = L/D_{eff} > 5$ (Saxena et al., 2018), where
739 L is a digital rock (i.e., domain) length, and D_{eff} is the effective grain diameter (e.g., Říha et al., 2018). For
740 S3 sub-volumes with $L = 875 \mu\text{m}$ REV size and $D_{eff} = 58.6 \mu\text{m}$ (computed from laboratory grain size data
741 which includes both sand and fines, Figure 6), this requirement is achieved as well: $N_{REV} = 15 > 5$, which
742 also proves the reliability of the sub-volume permeability modelling with the presented approach. The
743 calculations in sub-volume performed with Comsol (Eq. 7, Table 2) demonstrate the smallest deviation in
744 mean permeability compared to that in the full sample (0.85 %). In comparison, other sub-volumes modelled
745 with GeoDict (Figure 16) have larger mean permeability deviations from the full sample (ranging between 5
746 % and 17 %), still demonstrating a very good agreement with those conducted on the full-scale S3 domain.

747 Further, according to Saxena et al. (2018), REV size supported by N_{REV} for flow simulations, should
748 also be insensitive to the choice of boundary conditions, which effect on tensorial flow properties diminishes
749 with an increasing sample size (e.g., Guibert et al., 2016; Gerke et al., 2019). No-slip boundary conditions
750 applied in our study at four lateral faces of the modelling domains, correspond to those in the experimental
751 permeability measurements and are also the most commonly used boundary conditions for the pore-scale flow
752 simulations (Guibert et al., 2016 and references therein). However, they were recently shown to suppress the
753 transversal flow through the simulation domain to some extent, resulting in deviation in alignment of the
754 permeability tensor and in underestimation of its magnitude (Gerke et al., 2019) even at REV dimensions.
755 Thus, the difference in the mean permeability derived from all REV-sized sub-volumes ($\sim 4381 \text{ mD}$) and that
756 simulated over the entire S3 geometry ($\sim 4500 \text{ mD}$) (Figure 16) can also be attributed to this effect. For the
757 future studies we suggest that determining REV size for the flow simulation from porosity is justified, by
758 acknowledging the typical ratio of two between those for permeability and porosity.

759 To upscale to permeability reliably, the REV domain should be sufficiently large such that it is bounded
760 from below by the scale of the textural bedding but should not be larger than necessary to optimize the
761 computational efficiency (while remaining within the same scale of heterogeneity, i.e., at the macro scale). As
762 a result, a REV with an edge length of $\sim 2950 \mu\text{m}$ was chosen in the current study in sample S1, based on slice-
763 by-slice porosity profiles that reveal mm-scale layering in the z-direction (Figure 11c), rather than on the
764 classic isotropic REV approach. For comparison, in other studies, the edge lengths of REV in sandstones were
765 0.68 mm (Ovaysi and Piri, 2010), 0.8 mm (Mostaghimi et al., 2012), and 1.2 mm (Okabe and Oseto, 2006;
766 Tatomir et al., 2016) derived by the classic approach. In contrast to the classic REV estimation, where porosity

767 analysis does not consider directionality, 1D profiles from slice-by-slice porosity provides additional
768 information on anisotropy and inhomogeneity of the sample which have implications on the ultimate
769 determination of the REV. In the future studies, the 1D profiles can be used to calculate spatial correlation
770 length (e.g., using variogram analyses) of geological structures that include layering, as in S1 in the current
771 study.

772 Another source of inaccuracy is the geometry used for the flow model. The geometry considered in this
773 study included only the pore network connecting six faces of the REV cube. Other pore spaces in the REV
774 disconnected from the main network were deleted (because all paths smaller than the resolution were
775 prescribed as grain pixels due to the partial volume effect), thus resulting in the smaller effective size of the
776 simulation domain. The image porosity of sample S1 was 17.5 %, whereas its connected porosity was
777 estimated as 15.6 % (Table 3), while those of sample S3 were 28.3 % and 27.9 %, respectively.

778 Furthermore, the mesh was generated by taking a trade-off between the size of the mesh elements (4
779 elements in the smallest pore throat) and computational limits into account, while coarsening the mesh
780 elements towards the pore centre. The connectivity between pores with very fine pore throats that could not
781 be replaced by mesh elements could be lost, resulting in the loss of those pores in the calculations. In sample
782 S1, the porosity used in the simulation was approximately 50 % smaller than the porosity estimated by gas
783 porosimetry (Tables 2, 3). In contrast, the porosity used in the simulations in S3 was mostly preserved,
784 comprising ~84 % of that estimated in the laboratory.

785 For comparison, in the fine-grained sample of the Lower Cretaceous sandstone from Heletz Field in
786 Israel (Figure 1a), which has grain size characteristics similar to those of S1 but with higher clay and additional
787 calcite contents (Tatomir et al., 2016), the permeability upscaled from micro-CT flow modelling (conducted
788 by the same simulation method as that in the current study) exceeded the gas permeability by a factor of ~7.
789 This could be related to the reduction in the specific surface area by image processing and meshing
790 (Mostaghimi et al., 2012) conducted for the flow modelling.

791 Finally, the upscaling process from the flow modelling successfully predicted the permeability
792 anisotropy ratio of ~ 2.3 in S1, as discussed above. For comparison, the permeability anisotropy ratio evaluated
793 using micro-CT flow monitoring in clay-free sandstones (Clavaud et al., 2008) had a mean value of ~2.5
794 (ranging from ~1.7 to ~5.2), related to the presence of less permeable silty layers. This is consistent with the

795 ratio estimated at the pore scale in Rothbach sandstone (~5) (Louis et al., 2005), attributed to lamination due
796 to differences both in the characteristics of the solid phase (grain size and packing) and in the content of the
797 Fe-ox.

798

799 **6. Conclusions**

800 This paper presents a detailed description and evaluation of a multi-methodological petrophysical approach
801 for the comprehensive multiscale characterization of reservoir sandstones. The validation was performed on
802 samples from three different consecutive layers of Lower Cretaceous sandstone in northern Israel. The
803 following conclusions can be drawn:

- 804 1. The suggested methodology enables the identification of links between Darcy-scale permeability
805 and an extensive set of geometrical, textural and topological rock descriptors. Specifically,
806 micro-scale geometrical rock descriptors (grain and pore size distributions, pore throat size,
807 characteristic length, pore throat length of maximal conductance, specific surface area, and
808 connectivity index) and macro-scale petrophysical properties (porosity and tortuosity), along
809 with anisotropy and inhomogeneity, are used to predict the permeability of the studied layers.
- 810 2. Laboratory porosity and permeability measurements conducted on centimetre-scale samples
811 show less variability for the quartz arenite (top and bottom) layers and more variability for the
812 quartz wacke (intermediate) layer. The magnitudes of this variability in the samples are correlated
813 with the dimensions of their representative volumes and anisotropy, both of which are evaluated
814 within the micro-CT-imaged 3D pore geometry. This variability is associated with clay and
815 cementation patterns in the layers.
- 816 3. Two different porosity variation patterns are revealed in the top quartz arenite layer: fluctuations
817 at ~100 μm half wavelength in all direction, associated with an average pore cross-section, and
818 those at ~3.5 mm wavelength in the vertical direction only, associated with the occurrence of
819 high- and low-porosity horizontal bands occluded by Fe-ox cementation. The latter millimetre-
820 scale variability is found to control the macroscopic rock permeability measured in the

laboratory. Bands of lower porosity could be generated by Fe-ox cementation in regions with higher surface areas adjacent to preferential fluid flow paths.

4. More heterogeneous pore structures were revealed in the quartz wacke sandstone of the intermediate layer. This heterogeneity resulted mainly from the presence of patchy clay deposition structure.
5. Quartz arenite sandstone of the bottom layer shows stationarity in the investigated domain and lower anisotropy characteristics than that of the top layer, due to less horizontal cement bands.
6. The macroscopic permeability upscaled from the pore-scale velocity field simulated by flow modelling in the micro-CT-scanned geometry of millimetre-scale sample shows agreement with laboratory petrophysical estimates obtained for centimetre-scale samples for the quartz arenite layers. Comparison of permeability tensors evaluated in multiple REV sub-volumes and in the full segmented sample of the bottom layer, shows a particular agreement attributed to the homogeneity of this sample.
7. The multi-methodological petrophysical approach detailed and evaluated in this study allows the accurate petrophysical characterization of reservoir sandstones with broad ranges of textural and topological features.

Acknowledgements

This project was supported by fellowships from the Ministry of Energy, Israel, and the University of Haifa. The authors are grateful to Igor Bogdanov from the University of Pau for his continuing scientific support. Special thanks to Rudy Swennen and his group from KU Leuven for their contributions to the MIP, thin section preparation, microscopy and micro-CT image processing; to Veerle Cnudde and her group from Ghent University for teaching us the image processing techniques; to Kirill Gerke and Timofey Sizonenko from the Russian Academy of Sciences for providing their image processing code; to Uzi Saltzman from Engineering Geology and Rock Mechanics Company, Israel, for sending his detailed historic geological description of the study area; and to Or Bialik, Nimer Taha and Ovie Emmanuel Eruteya from the University of Haifa, Israel, for their assistance in the laboratory work. We thank the editor and two anonymous reviewers for their significant contribution in enhancing this paper.

850 **Competing interests**

851 The authors declare that they have no conflicts of interest.

852

853 **Author contributions**

854 PH and RK designed the study. PH developed codes for pore-scale modelling with contributions by RK and
855 MH. BS advised the microscopy and led the geological interpretations. MH scanned the samples. NW led the
856 laboratory measurements. All co-authors participated in the analysis of the results. PH wrote the text with
857 contributions from all co-authors. All co-authors contributed to the discussion and revisions and approved the
858 paper.

859

860 **Supplementary Material & Data Availability**

861 3-D μ -CT datasets are freely available at the open access data repository “PANGAEA” under the given doi:
862 <https://doi.pangaea.de/10.1594/PANGAEA.907552>.

863

864 References

- 865 Abed, A. M.: Depositional environments of the early cretaceous Kurnub (Hatira) sandstones, North Jordan,
866 Sedimentary Geology, 31(3-4), 267-279, **1982**.
- 867 Akinlotan, O.: Porosity and permeability of the English (Lower Cretaceous) sandstones, Proceedings of the
868 Geologists' Association, 127, 681-690, **2016**.
- 869 Akinlotan, O.: Mineralogy and palaeoenvironments: the Weald Basin (Early Cretaceous), Southeast England,
870 The Depositional Record, 3(2), 187-200, **2017**.
- 871 Akinlotan, O.: Multi-proxy approach to palaeoenvironmental modelling: the English Lower Cretaceous Weald
872 Basin, Geol. J. 53, 316–335, **2018**.
- 873 Ambegaokar, V., Halperin, B. I., & Langer, J. S. (1971). Hopping conductivity in disordered systems. *Physical*
874 *review B*, 4(8), 2612.
- 875 American Petroleum Institute, API : Recommended Practices for Core Analysis, RP 40, second edition, **1998**.
- 876 Amireh, B. S.: Sedimentology and palaeogeography of the regressive-transgressive Kurnub Group (Early
877 Cretaceous) of Jordan, Sedimentary Geology, 112(1-2), 69-88., **1997**.
- 878 Andrä, H., Combaret, N., Dvorkin, J., Glatt, E., Han, J., Kabel, M., Keehm. Y., Krzikalla, F., Lee, M.,
879 Madonna, C., Marsh, M., Mukerji, T., Saenger, E., Sain, R., Saxena, N., Ricker, S., Wiegmann, A., and
880 Zhan, X.: Digital rock physics benchmarks-Part I: Imaging and segmentation, Computers & Geosciences,
881 50, 25-32, **2013a**.
- 882 Andrä, H., Combaret, N., Dvorkin, J., Glatt, E., Han, J., Kabel, M., Keehm. Y., Krzikalla, F., Lee, M.,
883 Madonna, C., Marsh, M., Mukerji, T., Saenger, E., Sain, R., Saxena, N., Ricker, S., Wiegmann, A., and
884 Zhan, X.: Digital rock physics benchmarks-Part II: Computing effective properties, Computers &
885 Geosciences, 50, 33-43, **2013b**.
- 886 Arns, J.Y., Sheppard, A.P., Arns, C.H., Knackstedt, M.A., Yelkhovsky, A., and Pinczewski, W.V.: Pore-level
887 validation of representative pore networks obtained from micro-CT images. In: Proceedings of the annual
888 symposium of the society of core analysis, SCA2007-A26, Calgary, Canada, **2007**.
- 889 Asakawa, S., Watanabe, T., Lyu, H., Funakawa, S. and Toyohara, H.: Mineralogical composition of tidal flat
890 sediments in Japan, Soil Science and Plant Nutrition, 1-9, **2020**.
- 891 Avigad, D., Kolodner, K., McWilliams, M., Persing, H., and Weissbrod, T.: Origin of northern Gondwana
892 Cambrian sandstone revealed by detrital zircon SHRIMP dating, Geology, 31(3), 227-230, **2003**.
- 893 Avigad, D., Sandler, A., Kolodner, K., Stern, R. J., McWilliams, M., Miller, N., and Beyth, M.: Mass-
894 production of Cambro-Ordovician quartz-rich sandstone as a consequence of chemical weathering of Pan-
895 African terranes: Environmental implications, Earth and Planetary Science Letters, 240(3-4), 818-826,
896 **2005**.
- 897 Bear, J.: Dynamics of fluids in porous media. Courier Corporation, **2013**.
- 898 Blunt, M. J., Bijeljic, B., Dong, H., Gharbi, O., Iglauer, S., Mostaghimi, P., Paluszny, A., and Pentland, C.:
899 Pore-scale imaging and modelling, Advances in Water Resources, 51, 197-216, **2013**.
- 900 Boek, E. S., and Venturoli, M.: Lattice-Boltzmann studies of fluid flow in porous media with realistic rock
901 geometries, Computers & Mathematics with Applications, 59(7), 2305-2314, **2010**.

902 Bogdanov, I. I., Guerton, F., Kpahou, J., and Kamp, A. M.: Direct pore-scale modeling of two-phase flow
 903 through natural media, in: Proceedings of the 2011 COMSOL Conference in Stuttgart, **2011**.

904 Bogdanov, I. I., Kpahou, J., and Guerton, F.: Pore-scale single and two-phase transport in real porous medium,
 905 in: Proceedings of ECMOR XIII-13th European Conference on the Mathematics of Oil Recovery,
 906 September, **2012**.

907 Boudreau, B. P.: The diffusive tortuosity of fine-grained unlithified sediments, *Geochimica et Cosmochimica*
 908 *Acta*, 60(16), 3139-3142, **1996**.

909 Brabant, L., Vlassenbroeck, J., De Witte, Y., Cnudde, V., Boone, M. N., Dewanckele, J., and Van Hoorebeke,
 910 L.: Three-dimensional analysis of high-resolution X-ray computed tomography data with Morpho+,
 911 *Microscopy and Microanalysis*, 17(2), 252-263, **2011**.

912 Brunke, O., Brockdorf, K., Drews, S., Müller, B., Donath, T., Herzen, J., and Beckmann, F.: Comparison
 913 between X-ray tube based and synchrotron radiation based μ CT, in: *Developments in X-ray Tomography*
 914 VI, edited by: Stock, S. R., San Diego: SPIE, 7078, **2008**.

915 Callow, B., Falcon-Suarez, I., Marin-Moreno, H., Bull, J. M., and Ahmed, S. Optimal X-ray micro-CT image
 916 based methods for porosity and permeability quantification in heterogeneous sandstones, *Geophysical*
 917 *Journal International*, 223(2), 1210-1229, **2020**.

918 Calvo, R., The diagenetic history of Heletz Formation and the timing of hydrocarbons accumulation in Heletz-
 919 Kokhav oil field. M.Sc. thesis, The Hebrew University of Jerusalem, 72 p. (in Hebrew, with English
 920 abstract), **1992**.

921 Calvo, R., Ayalon, A., Bein, A., and Sass, E.: Chemical and isotopic composition of diagenetic carbonate
 922 cements and its relation to hydrocarbon accumulation in the Heletz-Kokhav oil field (Israel), *Journal of*
 923 *Geochemical Exploration*, 108(1), 88-98, **2011**.

924 Carman, P. C.: Fluid flow through granular beds, *Trans. Inst. Chem. Eng.*, 15, 150-166, **1937**.

925 Cerepi, A., Durand, C., and Brosse, E.: Pore microgeometry analysis in low-resistivity sandstone reservoirs,
 926 *Journal of Petroleum Science and Engineering*, 35(3-4), 205-232, **2002**.

927 Clavaud, J. B., Mainault, A., Zamora, M., Rasolofosaon, P., and Schlitter, C.: Permeability anisotropy and its
 928 relations with porous medium structure, *Journal of Geophysical Research: Solid Earth*, 113(B1), **2008**.

929 Cnudde, V., and Boone, M. N.: High-resolution X-ray computed tomography in geosciences: A review of the
 930 current technology and applications, *Earth-Science Reviews*, 123, 1-17, **2013**.

931 Cohen, A., and Boehm, S.: Lithofacies and environments of deposition of the Lower Cretaceous Helez &
 932 Telamim Formations, Geological Survey of Israel Report No. 5, **1983**.

933 Cohen, Z.: The geology of the Lower Cretaceous in Southern Coastal Plain, Ph.D. thesis, The Hebrew
 934 University of Jerusalem, 98 pp. (in Hebrew, with English abstract), **1971**.

935 Cressie, N.: Fitting variogram models by weighted least squares. *Journal of the international Association for*
 936 *mathematical Geology*, 17(5), 563-586, **1985**.

937 Du, S., Pang, S., and Shi, Y.: Quantitative characterization on the microscopic pore heterogeneity of tight oil
 938 sandstone reservoir by considering both the resolution and representativeness, *J. Pet. Sci. Eng.*, 169, 388-
 939 392, **2018**.

940 Dullien, F. A.: Porous media: fluid transport and pore structure, Academic press, **2012**.

941 Harter, T.: Finite-size scaling analysis of percolation in three-dimensional correlated binary Markov chain
 942 random fields, *Physical Review E*, 72(2), 026120, **2005**.

943 Farrel, N.J.C., Healy, D., and Taylor, C.W.: Anisotropy of permeability in faulted porous sandstones. *Journal*
 944 *of Structural Geology* 63, 50-67, **2014**.

945 Ferreira, N. N., Ferreira, E. P., Ramos, R. R., and Carvalho, I. S.: Palynological and sedimentary analysis of
 946 the Igarapé Ipiranga and Querru 1 outcrops of the Itapecuru Formation (Lower Cretaceous, Parnaíba
 947 Basin), Brazil, *Journal of South American Earth Sciences*, 66, 15-31, **2016**.

948 Folk, R. L., and Ward, W. C.: Brazos River bar [Texas]; a study in the significance of grain size parameters,
 949 *Journal of Sedimentary Research*, 27(1), 3-26, **1957**.

950 Gardosh, M. A., and Tannenbaum, E.: The petroleum systems of Israel, in: *Petroleum systems of the Tethyan*
 951 *region: AAPG Memoir*, edited by: Marlow, L., Kendall, C., and Yose, L., 106, 179-216, **2014**.

952 Garfunkel, Z.: The pre-quadernary geology in Israel, in: *The zoogeography of Israel*, edited by: Tchernov, E.,
 953 and Yom-Tov, Y., Dr W. Junk Publishers, Dordrecht, Netherlands, 7-34, **1988**.

954 Garfunkel, Z.: History and paleogeography during the Pan-African orogen to stable platform transition:
 955 reappraisal of the evidence from the Elat area and the northern Arabian-Nubian Shield, *Israel Journal of*
 956 *Earth Sciences*, 48, 135-157, **1999**.

957 Gerke, K. M., Karsanina, M. V., and Katsman, R.: Calculation of tensorial flow properties on pore level:
 958 Exploring the influence of boundary conditions on the permeability of three-dimensional stochastic
 959 reconstructions, *Physical Review E*, 100, 053312, **2019**.

960 Giesche, H.: Mercury porosimetry: a general (practical) overview. *Particle & particle systems characterization*,
 961 23(1), 9-19, **2006**.

962 Grader, P., and Reiss, Z.: On the Lower Cretaceous of the Heletz area, *Geological Survey of Israel, Bull No.*
 963 16, 14 pp., **1958**.

964 Grader, P.: The geology of the Heletz oil field, Ph.D. thesis, The Hebrew University of Jerusalem, 81 pp. (in
 965 Hebrew, with English abstract), **1959**.

966 Gringarten, E., and Deutsch, C.V.: Teacher's aide semivariogram interpretation and modeling. *Mathematical*
 967 *Geology*, 33(4), 507-534, **2001**.

968 Guibert, R., Horgue, P., Debenest, G., and Quintard, M.: A comparison of various methods for the numerical
 969 evaluation of porous media permeability tensors from pore-scale geometry, *Mathematical Geosciences*,
 970 48(3), 329-347, **2016**.

971 Haldorsen, H. H., and Lake, L. W.: A new approach to shale management in field-scale models, *Society of*
 972 *Petroleum Engineers Journal*, 24(04), 447-457, **1984**.

973 Halisch, M.: Application and assessment of the lattice boltzmann method for fluid flow modeling in porous
 974 rocks, PhD thesis, Technical University of Berlin, 182 pp., **2013a**.

975 Halisch, M.: The REV Challenge – estimating representative elementary volumes and porous rock
 976 inhomogeneity from high resolution micro-CT data sets, *Society of Core Analysts (SCA) Proceedings*,
 977 SCA2013-069, **2013b**.

978 Halisch, M., Weller, A., Debschütz, W., Sattler, C. D., and El-Sayed, A. M.: A complex core-log case study
979 of an anisotropic sandstone, originating from Bahariya Formation, Abu Gharadig Basin, Egypt,
980 *Petrophysics*, 50(06), **2009**.

981 Haoguang, W. E. I., Kun, M. A., Xiang'an, Y. U. E., and Xinxin, W. A. N. G.: The Relationship of Ultra-Low
982 Permeability Sandstone Aspect Ratio With Porosity, Permeability, *Advances in Petroleum Exploration*
983 and Development, 7(1), 7-12, **2014**.

984 Harding, T. G., Norris, B., and Smith, K.H.: Horizontal Water Disposal Well Performance in a High Porosity
985 and Permeability Reservoir Conference: SPE International Thermal Operations and Heavy Oil
986 Symposium and International Horizontal Well Technology Conference.
987 SPE-18153-MS, <https://doi.org/10.2118/79007-MS>, **2002**.

988 Hurst, A., and Nadeau, P. H.: Clay microporosity in reservoir sandstones: an application of quantitative
989 electron microscopy in petrophysical evaluation, *AAPG bulletin*, 79(4), 563-573, **1995**.

990 Iassonov, P., Gebrenegus, T., and Tuller, M.: Segmentation of X-ray computed tomography images of porous
991 materials: A crucial step for characterization and quantitative analysis of pore structures, *Water Resources*
992 *Research*, 45(9), **2009**.

993 Jackson, M. D., Muggeridge, A. H., Yoshida, S., and Johnson, H. D.: Upscaling permeability measurements
994 within complex heterolithic tidal sandstones, *Mathematical Geology*, 35(5), 499-520, **2003**.

995 Kalaydjian, F.: Origin and quantification of coupling between relative permeabilities for two-phase flows in
996 porous media, *Transport in porous media*, 5(3), 215-229, **1990**.

997 Kass, M., Witkin, A., and Terzopoulos, D.: Snakes: Active contour models, *International Journal of Computer*
998 *Vision*, 1(4), 321-331, **1988**.

999 Katz, A. J., and Thompson, A. H.: Prediction of rock electrical conductivity from mercury injection
1000 measurements, *Journal of Geophysical Research: Solid Earth*, 92(B1), 599-607, **1987**.

1001 Kerckhofs, G., Schrooten, J., Van Cleynenbreugel, T., Lomov, S. V., and Wevers, M.: Validation of x-ray
1002 micro-focus computed tomography as an imaging tool for porous structures, *Review of Scientific*
1003 *Instruments*, 79(1), 013711, **2008**.

1004 Khan, F., Enzmann, F., and Kersten, M.: Multi-phase classification by a least-squares support vector machine
1005 approach in tomography images of geological samples, *Solid Earth*, 7(2), 481-492, **2016**.

1006 Knackstedt, M., Jaime, P., Butcher, A.R., Botha, P.W.S.K., Middleton, J., and Sok, R.: Integrating reservoir
1007 characterization: 3D dynamic, petrophysical and geological description of reservoir facies. In:
1008 *Proceedings of the SPE Asia Pacific oil and gas conference and exhibition*, 18–20 October, 2010,
1009 Brisbane, Queensland, Australia, SPE 133981, **2010**.

1010 Kolodner, K., Avigad, D., Ireland, T. R., and Garfunkel, Z.: Origin of Lower Cretaceous ('Nubian') sandstones
1011 of North-east Africa and Arabia from detrital zircon U-Pb SHRIMP dating, *Sedimentology*, 56(7), 2010-
1012 2023, **2009**.

1013 Kozeny, J.: Über kapillare leitung der wasser in boden, *Royal Academy of Science, Vienna, Proceedings Class*
1014 *I*, 136, 271-306, **1927**.

1015 Krinsley, D. H., Pye, K., Boggs Jr, S., and Tovey, N. K.: Backscattered scanning electron microscopy and
1016 image analysis of sediments and sedimentary rocks. Cambridge University Press, **2005**.

1017 Lenormand, R.: Sca2003-52: Interpretation of mercury injection curves to derive pore size distribution, in:
1018 Proceedings of 2003 International Symposium of SCA., **2003**.

1019 Legland, D., Arganda-Carreras, I., Andrey, P.: MorphoLibJ: integrated library and plugins for mathematical morphology
1020 with ImageJ. *Bioinformatics*, 32(22), 3532-3534, **2016**.

1021 Li, Y., He, D., Chen, L., Mei, Q., Li, C., and Zhang, L.: Cretaceous sedimentary basins in Sichuan, SW China:
1022 Restoration of tectonic and depositional environments, *Cretaceous Research*, 57, 50-65, **2016**.

1023 Linden, S., Wiegmann, A., and Hagen, H.: The LIR space partitioning system applied to the Stokes equations,
1024 *Graph. Models* 82, 58–66 (2015).

1025 Linden S., Cheng L., Wiegmann A.: Specialized methods for direct numerical simulations in porous media,
1026 Math2Market GmbH, technical report, <https://doi.org/10.30423/report.m2m-2018-01>. **2018**.

1027 Liu, X., Wang, J., Ge, L., Hu, F., Li, C., Li, X., Yu, J., Xu, H., Lu, S., and Xue, Q.: Porescale characterization
1028 of tight sandstone in Yanchang Formation Ordos Basin China using micro-CT and SEM imaging from
1029 nm- to cm-scale, *Fuel*, 209, 254–264, **2017**.

1030 Lewis, J.J.M.: Outcrop-derived quantitative models of permeability heterogeneity for genetically different
1031 sand bodies. In: SPE Annual Technical Conference and Exhibition, 2-5 October 1988, Houston, Texas,
1032 **1988**.

1033 Louis, L., David, C., Metz, V., Robion, P., Menendez, B., and Kissel, C.: Microstructural control on the
1034 anisotropy of elastic and transport properties in undeformed sandstones. *International journal of rock*
1035 *mechanics and mining sciences*, 42(7-8), 911-923, **2005**.

1036 Massaad, M.: Origin and environment of deposition of Lebanon basal sandstones, *Eclogae Geologicae*
1037 *Helveticae*, 69(8), **1976**.

1038 Mckay, G., Use of Adsorbents for the Removal of Pollutants from Wastewater. CRC press, **1995**.

1039 MacKenzie, W. S., Adams, A. E., & Brodie, K. H. *Rocks and Minerals in Thin Section: A Colour Atlas*. CRC Press.,
1040 **2017**.

1041 Meyer, R., and Krause, F. F.: A comparison of plug-derived and probe-derived permeability in cross-bedded
1042 sandstones of the Virgelle Member, Alberta, Canada: The influence of flow directions on probe
1043 permeametry, *AAPG bulletin*, 85(3), 477-489, **2001**.

1044 Meyer, R.: Anisotropy of Sandstone Permeability. CREWES Research Report, Vol. 14, 2002.

1045 Mostaghimi, P., Blunt, M. J., and Bijeljic, B.: Computations of absolute permeability on micro-CT images,
1046 *Mathematical Geosciences*, 45(1), 103-125, **2012**.

1047 Moussavi-Harami, R., and Brenner, R. L.: Diagenesis of non-marine petroleum reservoirs: the Neocomian
1048 (Lower Cretaceous) Shurijeh Formation, Kopet-Dagh basin, NE Iran. *Journal of Petroleum Geology*,
1049 16(1), 55-72, **1993**.

1050 Munawar, M.J., Lin, C., Cnudde, V., Bultreys, T., Dong, C., Zhang, X., De Boever, W., Zahid, M.A., and Wu,
1051 Y.: Petrographic characterization to build an accurate rock model using micro-CT: case study on low-
1052 permeable to tight turbidite sandstone from Eocene Shahejie Formation, *Micron* 109, 22–33, **2018**.

1053 Narsilio, G. A., Buzzi, O., Fityus, S., Yun, T. S., and Smith, D. W.: Upscaling of Navier-Stokes equations in
1054 porous media: Theoretical, numerical and experimental approach, *Computers and Geotechnics*, 36(7),
1055 1200-1206, **2009**.

1056 Nelson, P. H.: Pore-throat sizes in sandstones, tight sandstones, and shales, AAPG bulletin, 93(3), 329-340,
 1057 **2009.**

1058 Neuzil, C. E.: Permeability of Clays and Shales, Annual Review of Earth and Planetary Sciences, 47, 247-273,
 1059 **2019.**

1060 Nordahl, K., and Ringrose, P. S.: Identifying the representative elementary volume for permeability in
 1061 heterolithic deposits using numerical rock models, Mathematical Geosciences, 40(7), 753, **2008.**

1062 Nordahl, K., Ringrose, P. S., and Wen, R.: Petrophysical characterisation of a heterolithic tidal reservoir
 1063 interval using a process-based modelling tool, Petroleum Geoscience, 11, 17-28, **2005.**

1064 Norris, R. J., and J. J. M. Lewis. The geological modeling of effective permeability in complex heterolithic
 1065 facies, in SPE Annual Technical Conference and Exhibition, Society of Petroleum Engineers, **1991.**

1066 Okabe, H., and Oseto, K.: Pore-scale heterogeneity assessed by the lattice-Boltzmann method, Society of Core
 1067 Analysts (SCA2006-44), 12-16, **2006.**

1068 Ovaysi, S., and Piri, M.: Direct pore-level modeling of incompressible fluid flow in porous media, Journal of
 1069 Computational Physics, 229(19), 7456-7476, **2010.**

1070 Pettijohn, F. J., Potter, P. E., and Siever, R.: Sand and Sandstone. Springer Verlag, 2nd ed., New York, **1987.**

1071 Ploner, A.: The use of the variogram cloud in geostatistical modelling. *Environmetrics: The official journal of*
 1072 *the International Environmetrics Society*, 10(4), 413-437, **1999.**

1073 Pyrcz, M. J., and Deutsch, C. V.: The whole story on the hole effect. Geostatistical Association of Australasia,
 1074 Newsletter, 18, 3-5, **2003.**

1075 Renard, P., Genty, A., and Stauffer, F.: Laboratory determination of the full permeability tensor, Journal of
 1076 Geophysical Research: Solid Earth, 106(B11), 26443-26452, **2001.**

1077 Reynolds, A. D.: Paralic reservoirs. Geological Society, London, Special Publications, 444(1), 7-34, **2017.**

1078 Říha, J., Petrula, L., Hala, M., and Alhasan, Z. Assessment of empirical formulae for determining the hydraulic
 1079 conductivity of glass beads, Journal of Hydrology and Hydromechanics, 66(3), 337-347, **2018.**

1080 Ringrose, P., and Bentley, M.: Reservoir Model Design: A Practitioner's Guide, Springer, 249 p. New York,
 1081 **2015.**

1082 Rootare, H. M., and Prenzlow, C. F.: Surface areas from mercury porosimeter measurements, The Journal of
 1083 physical chemistry, 71(8), 2733-2736, **1967.**

1084 RP40, A. P. I. (1960). API recommended practice for core-analysis procedure. *Edition, API, New York*, 12-13.

1085 Rustad, A. B., Theting, T. G., and Held, R. J.: Pore space estimation, upscaling and uncertainty modelling for
 1086 multiphase properties. In SPE Symposium on Improved Oil Recovery, Society of Petroleum Engineers,
 1087 **2008.**

1088 Saltzman, U.: Survey of the southeastern flanks of Mount Hermon, Tahal report (in Hebrew), **1968.**

1089 Sato, M., Panaghi, K., Takada, N., and Takeda, M.: Effect of Bedding Planes on the Permeability and
 1090 Diffusivity Anisotropies of Berea Sandstone, Transport in Porous Media, 127(3), 587-603, **2019.**

1091 Saxena, N., Hows, A., Hofmann, R., Alpak, F. O., Freeman, J., Hunter, S., and Appel, M. Imaging and
 1092 computational considerations for image computed permeability: operating envelope of digital rock
 1093 physics, Advances in Water Resources, 116, 127-144, **2018.**

1094 Schindelin, J., Arganda-Carreras, I., Frise, E., Kaynig, V., Longair, M., Pietzsch, T., Preibisch, S., Rueden,
 1095 C., Saalfeld, S., Schmid, B., Tinevez, J., White, D., Hartenstein, V., Eliceiri, K., Tomancak, P., and
 1096 Cardona, A.: Fiji: an open-source platform for biological-image analysis, *Nature methods*, 9(7), 676, **2012**.
 1097 Schlüter, S., Sheppard, A., Brown, K., and Wildenschild, D.: Image processing of multiphase images obtained
 1098 via X-ray microtomography: a review, *Water Resources Research*, 50(4), 3615-3639, **2014**.
 1099 Schmitt, M., Halisch, M., Müller, C., and Fernandes, C. P.: Classification and quantification of pore shapes in
 1100 sandstone reservoir rocks with 3-D X-ray micro-computed tomography, *Solid Earth*, 7(1), 285-300, **2016**.
 1101 Scholz, C., Wirner, F., Götz, J., Rüde, U., Schröder-Turk, G. E., Mecke, K., and Bechinger, C.: Permeability
 1102 of porous materials determined from the Euler characteristic, *Physical review letters*, 109(26), 264504,
 1103 **2012**.
 1104 Sethian, J. A.: A fast marching level set method for monotonically advancing fronts, *Proceedings of the*
 1105 *National Academy of Sciences*, 93(4), 1591-1595, **1996**.
 1106 Shaw, S. M.: Southern Palestine geological map on a Scale 1:250,000 with explanatory notes, *Palestine Geol.*
 1107 *Soc. Publ.*, Jerusalem, **1947**.
 1108 Shenhav, H.: Lower Cretaceous sandstone reservoirs, Israel: petrography, porosity, permeability, *AAPG*
 1109 *Bulletin*, 55(12), 2194-2224, **1971**.
 1110 Sheppard, A. P., Sok, R. M., and Averdunk, H.: Techniques for image enhancement and segmentation of
 1111 tomographic images of porous materials, *Physica A: Statistical mechanics and its applications*, 339(1-2),
 1112 145-151, **2004**.
 1113 Shimron, A. E.: Tectonic evolution of the southern Mount Hermon, *Geological Survey of Israel Report*,
 1114 *GSI/10/98*, **1998**.
 1115 Sneh, A., and Weinberger, R.: Geology of the Metula quadrangle, northern Israel: Implications for the offset
 1116 along the Dead Sea Rift, *Israel Journal of Earth Sciences*, 52, **2003**.
 1117 Sneh, A., and Weinberger, R.: Metula sheet 2-11, *Geology Survey of Israel, Ministry of Energy*, **2014**.
 1118 Tatomir, A. B., Halisch, M., Duschl, F., Peche, A., Wiegand, B., Schaffer, M., Licha, T., Niemi, A., Bensabat,
 1119 J., and Sauter, M.: An integrated core-based analysis for the characterization of flow, transport and
 1120 mineralogical parameters of the Heletz pilot CO₂ storage site reservoir, *International Journal of*
 1121 *Greenhouse Gas Control*, 48, 24-43, **2016**.
 1122 Stephens, D. B., Hsu, K. C., Prieksat, M. A., Ankeny, M. D., Blandford, N., Roth, T. Kelsey, J., Whitworth, J.
 1123 R.: A comparison of estimated and calculated effective porosity. *Hydrogeology Journal*, 6(1), 156-165,
 1124 **1998**.
 1125 Tiab, D., and Donaldson, E. C.: *Petrophysics: Theory and Practice of Measuring Reservoir Rock and Fluid*
 1126 *Transport Properties*, Elsevier, **2004**.
 1127 Tidwell, V. C., and Wilson, J. L.: Permeability upscaling measured on a block of Berea Sandstone: Results
 1128 and interpretation, *Mathematical Geology*, 31(7), 749-769, **1999**.
 1129 Vincent, L., and Soille, P.: Watersheds in digital spaces: an efficient algorithm based on immersion
 1130 simulations, *IEEE Transactions on Pattern Analysis & Machine Intelligence*, 6, 583-598, **1991**.

1131 Vogel, H. J.: Topological characterization of porous media, in: Morphology of condensed matter, edited by:
1132 Mecke, K. R., and Stoyan, D., Springer, Berlin, 75-92, **2002**.

1133 Wang, W. P., Liu, J. L., Zhang, J. B., Li, X. P., Cheng, Y. N., Xin, W. W., & Yan, Y. F. Evaluation of laser
1134 diffraction analysis of particle size distribution of typical soils in China and comparison with the Sieve-
1135 Pipette method. *Soil science*, 178(4), 194-204, **2013**.

1136 Viswanathan, J., Konwar, D., & Jagatheesan, K. Laboratory Characterization of Reservoir Rock and Fluids of
1137 Upper Assam Basin, India. In *Novel Issues on Unsaturated Soil Mechanics and Rock Engineering:
1138 Proceedings of the 2nd GeoMEast International Congress and Exhibition on Sustainable Civil
1139 Infrastructures, Egypt 2018–The Official International Congress of the Soil-Structure Interaction Group
1140 in Egypt (SSIGE)* (p. 179). Springer., **2018**.

1141 Weissbrod, T.: Stratigraphy and correlation of the Lower Cretaceous exposures across the Dead Sea Transform
1142 with emphasis on tracing the Amir Formation in Jordan, *Israel Journal of Earth Sciences*, 51(2), 55–78,
1143 **2002**.

1144 Weissbrod, T., and Nachmias, J.: Stratigraphic significance of heavy minerals in the late Precambrian-
1145 Mesozoic clastic sequence (“Nubian Sandstone”) in the Near East, *Sedimentary Geology*, 47(3-4), 263-
1146 291, **1986**.

1147 Whitaker, S.: Flow in porous media I: A theoretical derivation of Darcy's law, *Transport in porous media*, 1(1),
1148 3-25, **1986**.

1149 Wiegmann, A.: GeoDict, the Digital Material Laboratory - Easy-to-use - Powerful - Accurate, Whitepaper,
1150 **2019**, <https://doi.org/10.30423/WHITEPAPER.M2M-2019>

1151 Wildenschild, D., and Sheppard, A. P.: X-ray imaging and analysis techniques for quantifying pore-scale
1152 structure and processes in subsurface porous medium systems, *Advances in Water Resources*, 51, 217-
1153 246, **2013**.

1154 Zhang, D., Zhang, R., Chen, S., and Soll, W. E.: Pore scale study of flow in porous media: Scale dependency,
1155 REV, and statistical REV, *Geophysical research letters*, 27(8), 1195-1198, **2000**.

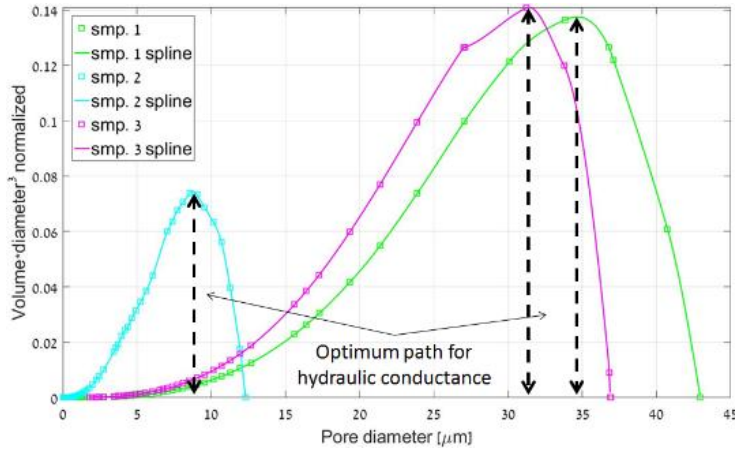
1156 Zhang, P., Leed, Y.I., and Zhange, J.: A review of high-resolution X-ray computed tomography applied to
1157 petroleum geology and a case study, *Micron*, 124, 102702, **2019**.

1158 Zhu, W., Montési, L.G.J., and Wong, T.F.: Effects of Stress on the Anisotropic Development of Permeability
1159 during Mechanical Compaction of Porous Sandstones, *Geological Society, London*, 119-136, Special
1160 Publications, 200, **2002**.

1161
1162
1163
1164
1165

1166

1167 Appendix A: Maximum hydraulic conductance



1168

1169 **Figure A1:** The pore throat length of the maximal hydraulic conductance, l_{max} , is defined from the maximal
1170 (normalized) hydraulic conductance (Katz and Thompson, 1987), specified at the vertical axis of the chart.
1171 The corresponding pore throat diameters (x-axis) marked by black arrows define the pore throat diameters
1172 (or pore throat lengths of maximal conductance), l_{max} , where all connected paths composed of $l \geq l_{max}$
1173 contribute significantly to the hydraulic conductance (see Sect.3.2).

1174

1175

1176